

Article

System Modeling and Simulation for Investigating Dynamic Characteristics of Geared Symmetric System Based on Linear Analysis

Joo-Mi Bahk, Sun-Hak Kim and Jong-Yun Yoon *

Department of Mechatronics Engineering, Incheon National University, (Songdo-dong) 119 Academy-ro, Yeonsu-gu, Incheon 22012, Republic of Korea; bahkm@inu.ac.kr (J.-M.B.); sunhak@inu.ac.kr (S.-H.K.)

* Correspondence: yoon3932@inu.ac.kr; Tel.: +82-32-835-8682

Abstract: Complex vibrational phenomena, such as gear impacts and mesh stiffness excitations, often require a significant amount of effort to be revealed using nonlinear analytical methods. However, key parameters for addressing vibrational problems can often be identified through simplified approaches based on linear analysis models. In light of these considerations, this study aimed to propose linear analytical methods to investigate the influences of various key parameters within symmetric systems. To achieve the main goal of this study, system modeling and eigensolutions were first implemented, focusing on a specific manual transmission with a front-engine/front-wheel configuration. Second, analytical techniques to reduce the number of degrees of freedom from the original symmetric system were suggested, and the reduced model was validated. Third, the system responses in the time domain were examined, along with key system parameters, such as gear mesh stiffness and clutch dampers, using state-variable equations. As a result, the findings from the linear system model demonstrated the fundamental dynamic characteristics of the torsional system within specific frequency regimes relevant to noise and vibration problems. Furthermore, the reduced lumped linear model employing the state-variable formula established its reliability in determining key parameters for mitigating noise and vibration problems.

Keywords: geared system; manual transmission; driveline; linear analysis; eigensolutions; system reduction; symmetrically torsional system; state-variable equation



Citation: Bahk, J.-M.; Kim, S.-H.; Yoon, J.-Y. System Modeling and Simulation for Investigating Dynamic Characteristics of Geared Symmetric System Based on Linear Analysis. *Symmetry* **2023**, *15*, 1904. <https://doi.org/10.3390/sym15101904>

Academic Editors: Yunqing Tang, Kun Xu and Bing Yang

Received: 21 September 2023

Revised: 6 October 2023

Accepted: 9 October 2023

Published: 11 October 2023



Copyright: © 2023 by the authors. Licensee MDPI, Basel, Switzerland. This article is an open access article distributed under the terms and conditions of the Creative Commons Attribution (CC BY) license (<https://creativecommons.org/licenses/by/4.0/>).

1. Introduction

In the field of system dynamics, which focuses on torsional vibrations occurring in a vehicle driveline with symmetric conditions, numerous studies have been conducted to improve noise, vibration, and harshness (NVH) qualities [1–22]. These studies have aimed to identify the main causes of NVH problems, such as gear rattle and whine noise, by comprehending the basic mechanisms of drivelines with gear pairs and their dynamic characteristics through both linear and nonlinear analyses [10–13]. To determine the key parameters related to the specific noise and vibration issues, linear analysis can be performed as a fundamental step to reveal the critical system parameters relevant to the NVH problems in question [1–7]. When it comes to examining system responses, the analytical approach is commonly more efficient for diagnosing and improving vehicle driveline problems under symmetric conditions than the experimental method, as experiments generally require more significant costs and time than simulations [16–19].

In a review of prior studies, Yoon and Singh investigated the dynamic properties of gear rattle under wide-open throttle (WOT) and coast conditions. They proposed a simplified nonlinear model employing drag torque estimation [1]. Guo et al. suggested a prediction model for gear rattle incorporating various key parameters, such as backlash, time-varying mesh stiffness, nonlinear oil film force between teeth, and drag torque. In this study, the developed model was compared with experimental methods, revealing the

influence of each parameter on gear rattle [2]. Zhou et al. conducted experimental studies on the rattle behavior of a complete dual-clutch transmission (DCT) system, both on a rattle test bench and in a vehicle [3]. Through this study, the authors investigated the gear rattle sensitivity and the dynamic evolution of the geartrain in a DCT. Diez-Ibarbia et al. proposed examining the lubricant effect between teeth in contact to understand its role in non-stationary phenomena. In this context, the gear transmission model was used to calculate the dynamic transmission error (DTE), with a specific focus on the influence of fluid viscosity on the system's dynamic behavior [4]. Bozca proposed the method to reduce the gear-rattle noise of the five-speed manual gearbox with the optimization of gearbox geometric design parameters [5]. Rigaud and Perret-Liaudet investigated the nonlinear dynamic behavior of a rattling spur gear pair induced by vibro-impacts between gear teeth. They suggested their own experimental set-up to visualize the contact zone and identify the successive impacts [6]. Donmez and Kahraman proposed a gear rattle prediction model by incorporating manufacturing errors such as eccentricities and tooth indexing errors [7]. Singh et al. proposed design guidelines for automotive manual transmissions and discussed gear rattle criteria based on clutch, flywheel, and drag torque [8]. Pizzolante et al. proposed an analytical procedure for the generalization of the rattle index in any type of ordinary transmission layout. To determine the rattle index, they conducted numerical studies to examine the effectiveness and reliability of the introduced index [9]. Guo et al. suggested a comprehensive nonlinear model to investigate the effects of influencing parameters such as drag torque, nonlinear oil film force, lubricant viscosity, time-varying meshing stiffness, friction force, and gear backlash. This study demonstrated a nonlinear dynamic model of gear rattling that considered the combined effects of the aforementioned parameters and their severity [10]. Shangguan et al. presented a nonlinear torsional model for a driveline system with four degrees of freedom to study gear rattle under idling conditions [11]. In this study, they developed experimental and calculation methods to reduce gear rattle in a generic transmission at idle. Trochon suggested a lumped parameter model of an automotive manual transmission corresponding to a nonlinear system and compared neutral rattle phenomena under driving and coast conditions [12]. Idehara et al. conducted and verified a system model of a powertrain with gear pairs to reduce gear impacts by changing clutch disc parameters [13]. Beinstingel et al. investigated parametrically excited vibrations and parametric instabilities arising from time-varying gear mesh stiffness, resulting in gear whine [14]. In this study, the authors analyzed the nonlinear model using the Newmark integration scheme and the harmonic balance approach to identify parametric instabilities. Pizzolante et al. proposed an analytical formulation capable of forecasting the main overall direction and magnitude of bearing reaction forces on an idler gear under quasi-static conditions [15]. In this study, they aimed to examine the geartrain formed by three gears to observe the modification of the ellipse shape concerning the excitation frequency and different modal shapes. Palermo et al. introduced a transmission error (TE) measurement with respect to the traditional direct method to demonstrate that low-cost digital encoders can be successfully used together with the elapsed time method [16]. To verify this measurement, the authors exploited it to compare the theoretical and experimental methods. Mughal et al. introduced a gear tribodynamics model using the potential energy method to estimate time variable meshing stiffness (TVMS) [17]. In this research, the authors suggested a fully analytical and time-efficient model for lubricated contact stiffness based on transitions in the regimes of lubrication. Yoo et al. proposed a hybrid metal composite gear to reduce gear whine noise and evaluated dynamic transmission error (DTE) [18]. In this study, they investigated the effect of composite material in reducing DTE in a hybrid metal composite gear in which the tooth and hub were steel-based and the blank was composed of a composite material. Barthod et al. suggested an experimental gearbox model for characterizing the rattle threshold and noise caused by engine torque fluctuations, investigating the rattle threshold, influence of excitation, and geometrical gearbox parameters [19]. Cui et al. proposed an analytical algorithm for meshing stiffness relative to the gear peeling position based on the

energy method, comparing the effects on peeling length, depth, and width [20]. Chen et al. proposed matching models between the dual-mass flywheel (DMF) and power transmission system based on sensitivity and the natural frequency range, adjusting structural and resultant parameters to understand the dynamic characteristics using the torsional stiffness of the DMF [21]. Ren et al. suggested a high-speed vehicle model to obtain the gear meshing forces and investigated their effect on the gear transmission under high-speed conditions [22].

According to the summaries of prior research, there appears to be a lack of fundamental approaches for conducting linear analysis in symmetric driveline systems, even though Singh et al. suggested a linearized design guideline to address gear impact problems [8]. Furthermore, the reviewed articles conducted their work using nonlinear analytical methods and their own experimental setups to resolve gear impact vibration issues. However, these methods require a significant amount of effort and cost. Thus, to overcome the complexity associated with nonlinear analysis, this study proposes the use of linear analytical methods to investigate and determine gear impact problems and their relevant key parameters. Therefore, the specific objectives of this study were as follows: (1) to propose mathematical techniques for reducing the number of degrees of freedom (DOFs) by comparing eigensolutions and frequency response functions (FRFs) derived from the original system with the results obtained from the reduced model; (2) to investigate linear system responses in the time domain using state variable equations, which were compared with results obtained from key factors, such as magnitude and phase, in the FRFs. This approach aimed to present efficient methods for determining key parameters to reduce the specific noise and vibration problems with less effort compared with nonlinear analysis. To achieve these specific objectives, this study focused on a specific manual transmission with a front-engine/front-wheel driveline assembly. In addition, Figure 1 illustrates the analytical approach using linear analysis. For example, the system modeling process was conducted in the first step, followed by the development of the original and reduced system models. The verification of the reduced model, involving a comparison of dynamic characteristics, such as eigensolutions and FRFs, led to the state variable equations to reveal the system responses and the effectiveness of key parameters in the time domain. In the case study, the primary key parameters, such as K_c , I_{o5} , and K_g , were the focus, and their designations are announced later.

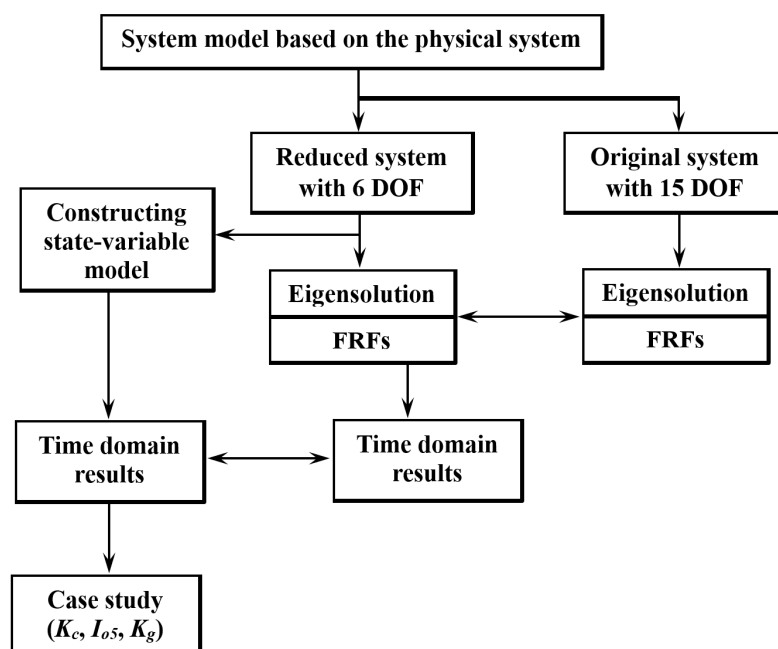


Figure 1. Flowchart of analytical approach for this study.

2. Problem Formulation

In this study, a specific manual transmission was analyzed under 3rd gear engaged and 5th gear unloaded condition within a front-engine/front-wheel drive configuration. Two models with 15 and 6 degrees of freedom (DOFs) were used for analysis [1]. Figure 2a depicts the physical driveline system with 15 DOFs. The power generated by the engine is transmitted from the flywheel and clutch to the tires through the transmission, as shown in Figure 2.

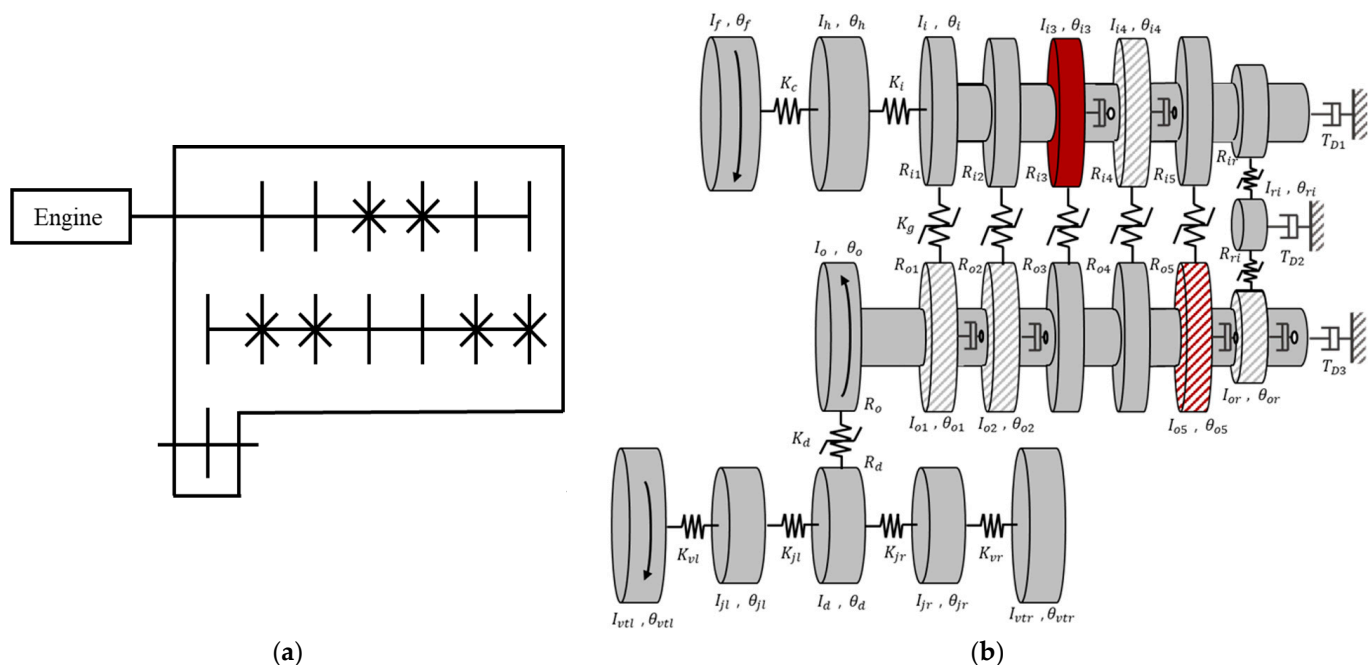


Figure 2. Schematic of driveline system with 15 DOFs: (a) physical driveline system [1]; (b) schematic diagram.

The manual transmission plays a crucial role in adapting the transferred torque and speed to suit various driving conditions. The transmission consists of three major components: input and output shafts, speed gears, and synchronizers. In Figure 2a, the symbols marked with a cross represent the speed gears, which remain unloaded and freely rotate unless the synchronizer is engaged. The straight lines in Figure 2a represent the fixed gears welded to the input (or output) shaft. Figure 2b provides a schematic diagram based on the physical system shown in Figure 2a. Each element in the schematic diagram is represented by lumped inertia or stiffness. The synchronizers and fixed gears are assumed to be lumped into the input and output shafts. The symbols and their descriptions for the lumped inertia and stiffnesses are summarized in Tables 1 and 2. To fulfill the objectives of this study, several assumptions were made: first, nonlinearities such as clutch hysteresis and gear backlashes were disregarded in the linear analysis. This omission removed the energy loss effect caused by dry friction and practical gear impact phenomena, respectively; second, gear pairs were assumed to be continuously in contact on the driving side, which always ensures a gear rattle-free condition; third, only one clutch stiffness value was considered, even though the clutch dampers exhibited multi-staged properties. This limitation prevented the exploration of gear impact conditions caused by changes in stiffness.

Table 1. Inertia employed in simulations.

Inertia (Description)	Values (kg·m ²)	Inertia	Values (kg·m ²)
I_f (Flywheel)	1.38×10^{-1}	I_{o5} (5th gear on output shaft)	5.23×10^{-4}
I_h (Clutch hub)	5.76×10^{-3}	I_{ri} (Idler)	4.35×10^{-4}
I_i (Input shaft)	3.10×10^{-3}	I_{or} (Reverse gear on output shaft)	1.33×10^{-3}
I_o (Output shaft)	25.33×10^{-3}	I_d (Differential)	2.15×10^{-2}
I_{i3} (3rd gear on input shaft)	5.80×10^{-4}	I_{jl} (Left cv joint)	3.91×10^{-3}
I_{i4} (4th gear on input shaft)	8.73×10^{-4}	I_{jr} (Right cv joint)	4.35×10^{-3}
I_{o1} (1st gear on output shaft)	2.60×10^{-3}	I_{vtl} (Left tire and vehicle)	23.9591
I_{o2} (2nd gear on output shaft)	1.39×10^{-3}	I_{vtr} (Right tire and vehicle)	23.9591

Table 2. Stiffness employed in simulations.

Stiffness (Description)	Values (N·m·rad ⁻¹)	Stiffness	Values (N·m ⁻¹)
K_i (Input shaft stiffness)	10,000	K_g (Gear mesh stiffness)	2.7×10^8
K_{jl}, K_{jr} (Stiffness between left or right drive shaft and differential)	10,000	K_d (Gear mesh stiffness between output shaft and differential)	2.7×10^8
K_{vl}, K_{vr} (Stiffness between left or right cv joint and vehicle)	10,000		
K_c (Clutch stiffness)	1838		

3. Modeling and Analysis of the Symmetric Driveline for Linear Analysis

3.1. Modeling of the Torsional System

The 15-DOF driveline system for this study consisted of several components, including the flywheel, clutch, driveshaft, joint, and vehicle, as shown in Figure 2b. Each of the elements depicted in Figure 2b represents lumped inertias and stiffnesses. The lumped mass, denoted I_f , is connected to the clutch hub, I_h , by the clutch stiffness, K_c . Using Newton's second law, Equation (1) can be derived as follows.

$$\sum_{i=1}^n T_i = -K_c(\theta_f - \theta_h) = I_f \ddot{\theta}_f \quad (1)$$

The torsional displacements of sub-systems connected with gear pairs are influenced by each gear ratio. The effect of these gear ratios should be incorporated into the mathematical formulation by considering the relative displacements in the gear pairs. The schematic for the clutch hub, input shaft, and speed gears is depicted in Figure 3a, where the inertia values of the 3rd gear and its relevant synchronizer are combined into the input shaft inertia, considering their engaged status. Figure 3b illustrates the basic mechanism with a free body diagram (FBD) that operates between gear pairs, such as the input shaft and speed gears on the output shaft, along with the torque flow. The torque transferred at the engaged gear pairs can be expressed as $R_{in}K_g\delta_n$. Here, $\delta_n = R_{in}\theta_{in} + R_{on}\theta_{on}$ represents the relative displacement of the speed gear pairs. The radius of each gear is summarized in Table 3.

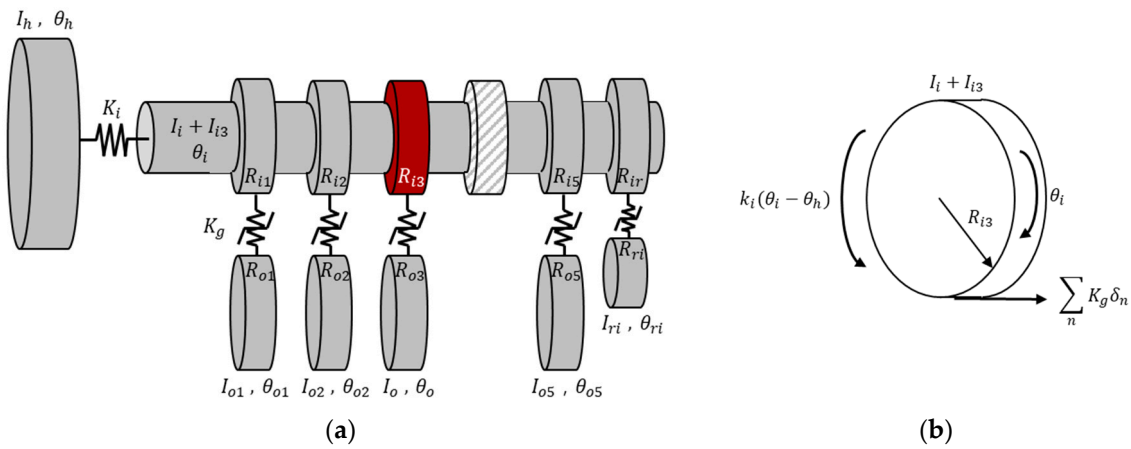


Figure 3. Schematic of the clutch hub, input shaft, and speed gears: (a) lumped masses with clutch hub, input shaft, and speed gears; (b) free body diagram of the input shaft.

Table 3. Gear radii employed in simulations.

Radius (Description)	Values (mm)	Radius	Values (mm)
R_{i1} (1st gear on input shaft)	18.30	R_{o2} (2nd gear on output shaft)	51.99
R_{i2} (2nd gear on input shaft)	29.51	R_{o3} (3rd gear on output shaft)	46.01
R_{i3} (3rd gear on input shaft)	35.50	R_{o4} (4th gear on output shaft)	39.55
R_{i4} (4th gear on input shaft)	41.95	R_{o5} (5th gear on output shaft)	35.58
R_{i5} (5th gear on input shaft)	45.92	R_{or} (Reverse gear on output shaft)	54.95
R_{ir} (Reverse gear on input shaft)	16.36	R_o (Final gear on output shaft)	26.63
R_{ri} (Idler)	40.14	R_d (Final gear on differential)	103.37
R_{o1} (1st gear on output shaft)	63.20		

As illustrated in Figure 3, the basic derivation of dynamic equations can be described as follows.

$$\sum_{i=1}^n T_i = -K_i(\theta_i - \theta_h) - K_g(R_{i1}\theta_{i1} + R_{o1}\theta_{o1})R_{i1} - K_g(R_{i2}\theta_{i2} + R_{o2}\theta_{o2})R_{i2} - K_g(R_{i5}\theta_{i5} + R_{o5}\theta_{o5})R_{i5} - K_g(R_{ir}\theta_i + R_{ri}\theta_{ri})R_{ir} - K_g(R_{i3}\theta_i + R_{o3}\theta_o)R_{i3} = (I_i + I_{i3})\ddot{\theta}_i \quad (2)$$

Thus, the complete equation of motion with 15 DOFs can be established as follows. Here, the torque excitation and damping effects are neglected for the implementation of the linear real eigensolutions, and $\underline{\theta}(t)$, \underline{M} , and \underline{K} represent the absolute torsional displacement, inertia, and stiffness matrices, respectively.

$$\underline{M} \ddot{\underline{\theta}}(t) + \underline{K} \underline{\theta}(t) = \underline{0}. \quad (3)$$

$$\underline{\theta} = [\theta_f \ \theta_h \ \theta_i \ \theta_o \ \theta_{01} \ \theta_{02} \ \theta_{o5} \ \theta_{ri} \ \theta_{or} \ \theta_{i4} \ \theta_d \ \theta_{jl} \ \theta_{jr} \ \theta_{vlt} \ \theta_{vtr}]^T. \quad (4)$$

$$\underline{\underline{M}} = \text{diag} \left[I_f, I_h, (I_i + I_{i3}), I_o, I_{o1}, I_{o2}, I_{o5}, I_{ri}, I_{or}, I_{i4}, I_d, I_{jl}, I_{jr}, I_{vtl}, I_{vtr} \right]. \quad (5)$$

$$\underline{\underline{K}} = \begin{bmatrix} & \\ & k(i,j) \\ & \end{bmatrix}. \quad (6)$$

$$k_{1,1} = k_c, \quad (7a)$$

$$k_{2,2} = k_c + k_i. \quad (7b)$$

$$k_{3,3} = k_i + k_g \left(R_{i1}^2 + R_{i2}^2 + R_{i3}^2 + R_{i5}^2 + R_{ir}^2 \right). \quad (8)$$

$$k_{4,4} = k_g \left(R_{o3}^2 + R_{o4}^2 \right) + k_d R_o^2. \quad (9)$$

$$k_{5,5} = k_g R_{o1}^2, \quad (10a)$$

$$k_{6,6} = k_g R_{o2}^2. \quad (10b)$$

$$k_{7,7} = k_g R_{o5}^2, \quad (11a)$$

$$k_{8,8} = 2k_g R_{ri}^2. \quad (11b)$$

$$k_{9,9} = k_g R_{or}^2, \quad (12a)$$

$$k_{10,10} = k_g R_{i4}^2. \quad (12b)$$

$$k_{11,11} = k_d R_d^2 + k_{jl} + k_{jr}. \quad (13)$$

$$k_{12,12} = k_{jl} + k_{vl}, \quad (14a)$$

$$k_{13,13} = k_{jr} + k_{vr}. \quad (14b)$$

$$k_{14,14} = k_{vl}, \quad (15a)$$

$$k_{15,15} = k_{vr}. \quad (15b)$$

$$k_{1,2} = k_{2,1} = -k_c, \quad (16a)$$

$$k_{2,3} = k_{3,2} = -k_i. \quad (16b)$$

$$k_{3,4} = k_{4,3} = k_g R_{i3} R_{o3}, \quad (17a)$$

$$k_{3,5} = k_{5,3} = k_g R_{i1} R_{o1}. \quad (17b)$$

$$k_{3,6} = k_{6,3} = k_g R_{i2} R_{o2}, \quad (18a)$$

$$k_{3,7} = k_{7,3} = k_g R_{i5} R_{o5}. \quad (18b)$$

$$k_{3,8} = k_{8,3} = k_g R_{ir} R_{ri}, \quad (19a)$$

$$k_{4,10} = k_{10,4} = k_g R_{i4} R_{o4}. \quad (19b)$$

$$k_{4,11} = k_{11,4} = k_g R_o R_d, \quad (20a)$$

$$k_{8,9} = k_{9,8} = k_g R_{ri} R_{or}. \quad (20b)$$

$$k_{11,12} = k_{12,11} = -k_{jl}, \quad (21a)$$

$$k_{11,13} = k_{13,11} = -k_{jr}. \quad (21b)$$

$$k_{12,14} = k_{14,12} = -k_{vl}, \quad (22a)$$

$$k_{13,15} = k_{15,13} = -k_{vr}. \quad (22b)$$

Here, the units K_g and K_d are in $\text{N}\cdot\text{m}^{-1}$, and the torsional stiffness has the unit of $\text{N}\cdot\text{m}\cdot\text{rad}^{-1}$.

3.2. Modal Analysis of the Torsional System

In general, the dynamic characteristics of a system were examined on the basis of the modal analysis, in which the natural frequencies and mode shapes reveal the fundamental dynamic behaviors of the system when it is excited. Consequently, the results from modal analysis provide the practical information necessary for improving vibratory conditions resulting from various excitation forces or torques. The characteristic equation of this system can be obtained by multiplying Equation (3) by the inverse inertia matrix $\underline{\underline{M}}^{-1}$ as follows [23–29].

$$\underline{\underline{M}}^{-1} \underline{\underline{M}} \ddot{\underline{\theta}}(t) + \underline{\underline{M}}^{-1} \underline{\underline{K}} \underline{\theta}(t) = \underline{0}. \quad (23)$$

$$\ddot{\underline{\theta}}(t) + \underline{\underline{M}}^{-1} \underline{\underline{K}} \underline{\theta}(t) = \underline{0}. \quad (24)$$

$$\underline{\theta}(t) = \underline{U} e^{i(wt+\phi)}. \quad (25)$$

$$\ddot{\underline{\theta}}(t) = -w^2 \underline{U} e^{i(wt+\phi)} = -\lambda \underline{U} e^{i(wt+\phi)}. \quad (26)$$

$$-\lambda \underline{U} e^{i(wt+\phi)} + \underline{\underline{M}}^{-1} \underline{\underline{K}} \underline{U} e^{i(wt+\phi)} = 0. \quad (27)$$

$$[-\lambda \underline{\underline{I}} + \underline{\underline{M}}^{-1} \underline{\underline{K}}] \underline{U} e^{i(wt+\phi)} = \underline{0}. \quad (28)$$

$$\underline{U} \neq 0, \det |\underline{\underline{M}}^{-1} \underline{\underline{K}} - \lambda \underline{\underline{I}}| = 0. \quad (29)$$

$$(\lambda - \lambda_1)(\lambda - \lambda_2) \cdots (\lambda - \lambda_r) \cdots (\lambda - \lambda_{15}) = 0, \quad \lambda_r = w_r^2, \quad r = 1, 2, \dots, 15. \quad (30)$$

$$\left[\underline{\underline{M}}^{-1} \underline{\underline{K}} - \lambda_r \underline{\underline{I}} \right] \underline{\underline{U}}_r = \underline{\underline{0}}. \quad (31)$$

$$\underline{\underline{K}} \underline{\underline{U}}_r = \lambda_r \underline{\underline{M}} \underline{\underline{U}}_r. \quad (32)$$

$$\left[\underline{\underline{U}} \right] = [\underline{\underline{U}}_1 \underline{\underline{U}}_2 \cdots \underline{\underline{U}}_r \cdots \underline{\underline{U}}_{15}]. \quad (33)$$

In this context, the general solution of Equation (24) can be expressed as Equation (25), where $\underline{\underline{U}}$ is an arbitrary constant vector with a size of 15 by 1, and ϕ represents an arbitrary phase. Here, $\lambda_r = w_r^2$ is an eigenvalue, and w_r is the corresponding natural frequency of the system. Eigenvectors corresponding to each eigenvalue are obtained from Equation (32), where $\underline{\underline{U}}_r$ represents the r th eigenvector. The modal matrix $\underline{\underline{U}}$ consists of each eigenvector augmented, as described in Equation (33). Therefore, each column vector projects its relevant mode shape for each concerned natural frequency. Mode shapes are vectors that represent the dynamic motions for each natural frequency, and the systems positioned after the output shaft, including the idler, are influenced by the gear ratio. For instance, concerning the output shaft, the torsional displacement is affected by the radii of R_{i3} and R_{o3} , which are related to the engagement of the 3rd gear. Consequently, the modal vector component $U_{(4,i)}$, which is associated with the output shaft, should be normalized considering the gear ratio, resulting in a modified modal vector $U_{(4,i)} \times \frac{R_{o3}}{R_{i3}}$. Considering the influence of the gear ratio for the rest of the sub-systems and normalizing the eigenvectors with respect to their maximum vector components yields the normalized modal vectors. The first four natural frequencies and mode shapes are presented in Table 4 and Figure 4. This study utilized MATLAB to obtain the results. Here, the y- and x-axes of Figure 3 are the normalized values of the modal vector and their relevant subsystem, as described in Equations (4) and (5). Considering the typical range of vehicle speeds, they do not exceed 8000 RPM, and at this speed, the firing frequency is below 300 Hz. Therefore, natural frequencies higher than 300 Hz were ignored. Additionally, since this torsional system is semi-positive definite, a rigid body mode appears, which must be disregarded due to numerical instabilities in the simulations [12,23–29].

Table 4. First four natural frequencies of the 15-DOF system.

Mode	Description	Natural Frequency (Hz)
1	Hopping mode (f_1)	2.3
2	Driveline surging mode (f_2)	7.6
3	Clutch spring mode (f_3)	60.8
4	Clutch + input shaft mode (f_4)	272.5

3.3. System Responses in the Frequency Domain

To obtain the frequency response functions (FRFs) based on the results calculated through modal analysis, damping effects must be included, as the real eigensolution is conducted without considering damping effects. Since it can be challenging to directly measure physical damping under dynamic conditions, the damping matrix can be reasonably approximated from the decoupled modal domain [12,23–29]. The mathematical formulation $\underline{\underline{P}}(t)$ as principal coordinates can be calculated by transferring the basic coordinates $\underline{\theta}(t)$, as follows.

$$\underline{\underline{M}} \ddot{\underline{\theta}}(t) + \underline{\underline{K}} \underline{\theta}(t) = \underline{\underline{0}}, \quad (34a)$$

$$\underline{\theta}(t) = \underline{\underline{U}} \underline{\underline{P}}(t). \quad (34b)$$

$$\underline{\underline{M}} \underline{\underline{U}} \ddot{\underline{P}}(t) + \underline{\underline{K}} \underline{\underline{U}} \underline{P}(t) = \underline{0}. \quad (35)$$

$$\underline{\underline{U}}^T \underline{\underline{M}} \underline{\underline{U}} \ddot{\underline{P}}(t) + \underline{\underline{U}}^T \underline{\underline{K}} \underline{\underline{U}} \underline{P}(t) = \underline{0}. \quad (36)$$

$$\underline{\underline{M}_r} \ddot{\underline{P}}(t) + \underline{\underline{K}_r} \underline{P}(t) = \underline{0}. \quad (37)$$

$$\begin{bmatrix} \ddots & & \\ & M_{ri} & \\ & & \ddots \end{bmatrix} \ddot{\underline{P}} + \begin{bmatrix} \ddots & & \\ & \lambda_i M_{ri} & \\ & & \ddots \end{bmatrix} \underline{P} = \underline{0}, \quad i = 1, 2, \dots, 15. \quad (38)$$

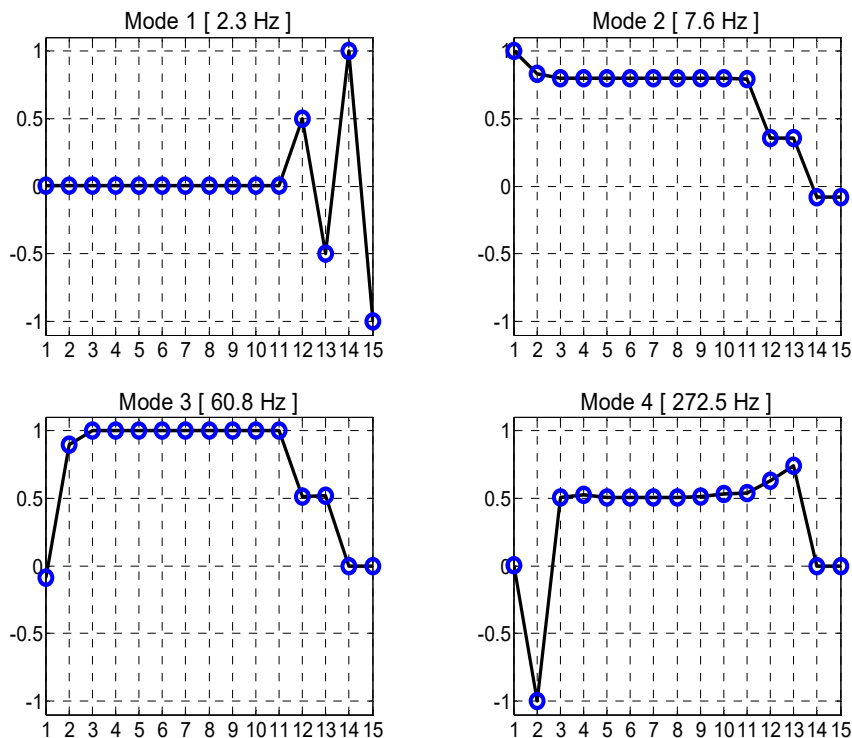


Figure 4. First four modes of the 15-DOF system.

Here, $\underline{\underline{M}_r}$ and $\underline{\underline{K}_r}$ represent the modal mass and stiffness matrices. Equation (38) describes the decoupled system, which is transformed into the modal coordinates $\underline{\eta}(t)$ from the physical coordinate system. From Equation (38), the normalized constant matrix $\underline{\underline{\beta}_r}$ is obtained as follows.

$$\underline{\underline{M}_r} = \begin{bmatrix} \ddots & & \\ & M_{ri} & \\ & & \ddots \end{bmatrix} = \begin{bmatrix} \ddots & & \\ & \sqrt{M_{ri}} & \\ & & \ddots \end{bmatrix} \begin{bmatrix} \ddots & & \\ & \sqrt{M_{ri}} & \\ & & \ddots \end{bmatrix}. \quad (39)$$

$$\underline{\underline{\beta}_r} = \underline{\underline{M}_r}^{\frac{1}{2}} = \begin{bmatrix} \ddots & & \\ & \sqrt{M_{ri}} & \\ & & \ddots \end{bmatrix}. \quad (40)$$

$$\underline{\underline{\beta}_r}^2 \ddot{\underline{P}}(t) + \underline{\underline{K}_r} \underline{P}(t) = \underline{0}, \quad \underline{P}(t) = \underline{\underline{\beta}_r}^{-1} \underline{\eta}(t). \quad (41)$$

$$\underline{\underline{\beta}}_r^{-1} \underline{\underline{\beta}}_r \underline{\underline{\beta}}_r \underline{\underline{\beta}}_r^{-1} \ddot{\underline{\eta}}(t) + \underline{\underline{\beta}}_r^{-1} \underline{\underline{K}}_r \underline{\underline{\beta}}_r^{-1} \underline{\eta}(t) = \underline{0}. \quad (42)$$

$$\ddot{\underline{\eta}}(t) + \begin{bmatrix} \ddots & & \\ & w_{ri}^2 & \\ & & \ddots \end{bmatrix} \underline{\eta}(t) = \underline{0}. \quad (43)$$

Here, Equation (43) clearly shows that the system is decoupled by reflecting its natural frequencies of the 15-DOF system. To transform the physical coordinate $\underline{\theta}(t)$ into the modal coordinate $\underline{\eta}(t)$, two stages of calculations are performed, as described in Equations (34)–(43), using the principal coordinate $\underline{P}(t)$. However, this transformation can be simplified into a stage, as follows.

$$\frac{1}{\sqrt{M_{ri}}} \underline{U}_i^T \underline{\underline{M}} \underline{U}_i \frac{1}{\sqrt{M_{ri}}} = 1, \quad i = 1, 2, 3, \dots, 15. \quad (44)$$

$$\underline{\underline{\phi}} = [\underline{U}_1 \quad \underline{U}_2 \quad \dots \quad \underline{U}_{15}] \begin{bmatrix} \frac{1}{\sqrt{M_{r1}}} & & & \\ & \frac{1}{\sqrt{M_{r2}}} & & \\ & & \ddots & \\ & & & \frac{1}{\sqrt{M_{r15}}} \end{bmatrix} = \underline{\underline{U}} \underline{\underline{\beta}}. \quad (45)$$

$$\underline{\underline{M}} \ddot{\underline{\theta}}(t) + \underline{\underline{K}} \underline{\theta}(t) = \underline{0}, \quad \underline{\theta}(t) = \underline{\underline{\phi}} \underline{\eta}(t). \quad (46)$$

$$\underline{\underline{M}} \underline{\underline{\phi}} \ddot{\underline{\eta}}(t) + \underline{\underline{K}} \underline{\underline{\phi}} \underline{\eta}(t) = \underline{0}. \quad (47)$$

$$\underline{\underline{\phi}}^T \underline{\underline{M}} \underline{\underline{\phi}} \ddot{\underline{\eta}}(t) + \underline{\underline{\phi}}^T \underline{\underline{K}} \underline{\underline{\phi}} \underline{\eta}(t) = \underline{0}. \quad (48)$$

$$\ddot{\eta}_r + w_r^2 \eta_r(t) = 0, \quad r = 1, 2, 3, \dots, 15. \quad (49)$$

Here, $\underline{\underline{\phi}}$ is the normal modal matrix, and Equations (44)–(49) represent the series of techniques for transforming the physical coordinates into the modal domain. Using the normal modal matrix $\underline{\underline{\phi}}$, the viscous damping matrix can be approximated as follows.

$$\underline{\underline{\phi}}^T \cdot \underline{\underline{C}} \cdot \underline{\underline{\phi}} = \begin{bmatrix} \ddots & & \\ & C_r & \\ & & \ddots \end{bmatrix} = \begin{bmatrix} \ddots & & \\ & 2\zeta w_r & \\ & & \ddots \end{bmatrix}. \quad (50)$$

$$[C] = [\phi^T]^{-1} \begin{bmatrix} \ddots & & \\ & 2\zeta_r w_r & \\ & & \ddots \end{bmatrix} [\phi]^{-1}. \quad (51)$$

$$\underline{\underline{M}} \ddot{\underline{\theta}}(t) + \underline{\underline{C}} \dot{\underline{\theta}}(t) + \underline{\underline{K}} \underline{\theta}(t) = \underline{T}(t). \quad (52)$$

$$\underline{T}(t) = [T \ 0 \ 0 \ 0 \ 0 \ 0 \ 0 \ 0 \ 0 \ 0 \ 0 \ 0 \ 0 \ 0 \ 0]^T. \quad (53)$$

$$\underline{\theta}(t) = \tilde{\underline{\theta}} e^{i\omega t}, \quad (54a)$$

$$\dot{\underline{\theta}}(t) = i \cdot \underline{w} \cdot \tilde{\underline{\theta}} e^{i\omega t}, \quad (54b)$$

$$\ddot{\underline{\theta}}(t) = -w^2 \cdot \tilde{\underline{\theta}} e^{i\omega t}. \quad (54c)$$

$$\left[\underline{\underline{K}} - \underline{\underline{M}} \cdot w^2 + i \underline{\underline{C}} w \right] \tilde{\underline{\theta}} e^{i\omega t} = \tilde{\underline{T}} e^{i\omega t}. \quad (55)$$

$$\tilde{\underline{\theta}}(w) = \left[\underline{\underline{K}} - \underline{\underline{M}} w^2 + i \underline{\underline{C}} w \right]^{-1} \tilde{\underline{T}}. \quad (56)$$

In this context, the damping matrix $\underline{\underline{C}}$ can be inversely derived reversely from the modal damping matrix C_r . In this study, a damping ratio ζ of 5% was employed, and Equation (52) represents the fundamental equation, incorporating the calculated physical damping matrix and its input torque vector. The excitation value for the input torque \underline{T} is set to unity. From Equation (56), the FRFs of the 15-DOF system can be calculated. The FRFs in the 15-DOF system described in Figure 5 are defined as follows: $|Y_{ff}|$, FRFs of the flywheel; $|Y_{hf}|$, FRFs of the clutch hub; $|Y_{if}|$, FRFs of the input shaft. The resonance regions in the FRFs depicted in Figure 5 correlate well with the natural frequencies obtained from the modal analysis.

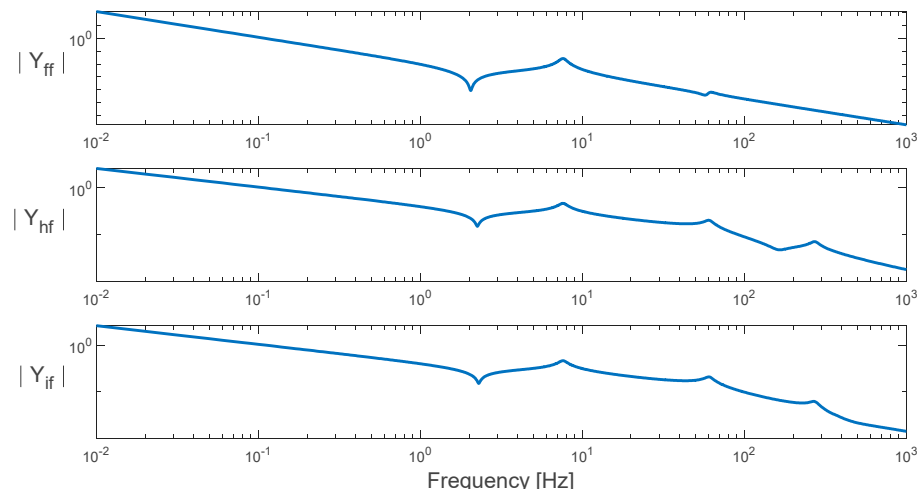


Figure 5. First three FRFs of 15-DOF model.

4. System Reduction and Validation with the Original System

The previously developed 15-DOF system model provides all dynamic characteristics, such as natural frequencies and resonance areas. However, the size of matrices and vectors in its mathematical formulations can lead to various issues in numerical simulations, including inefficient calculation times and convergence problems in numerical iterations, especially concerning sensitive nonlinearities [30]. To increase the reliability and efficiency of simulations, particularly when dealing with highly nonlinear elements such as gear impacts and parameter excitations in gear pairs, it is necessary to reduce the number of DOFs. To achieve the primary goal of this study, we focused on reducing the DOFs from 15 to 6 using a two-step process. First, the speed gears, which were not currently relevant for the examination, were lumped together with each driving input or output shaft. For instance, the 4th speed gear (or 1st, 2nd, and reverse gears) could be combined with the output shaft (or input shaft), as shown in Figures 2, 6 and 7 by considering their gear ratios, as illustrated in Figure 6 [31]. Second, the rotational system from the final gear to the wheel was simplified by distributing the inertia and stiffness values on the driveshaft equally, as illustrated in Figure 8 [32].

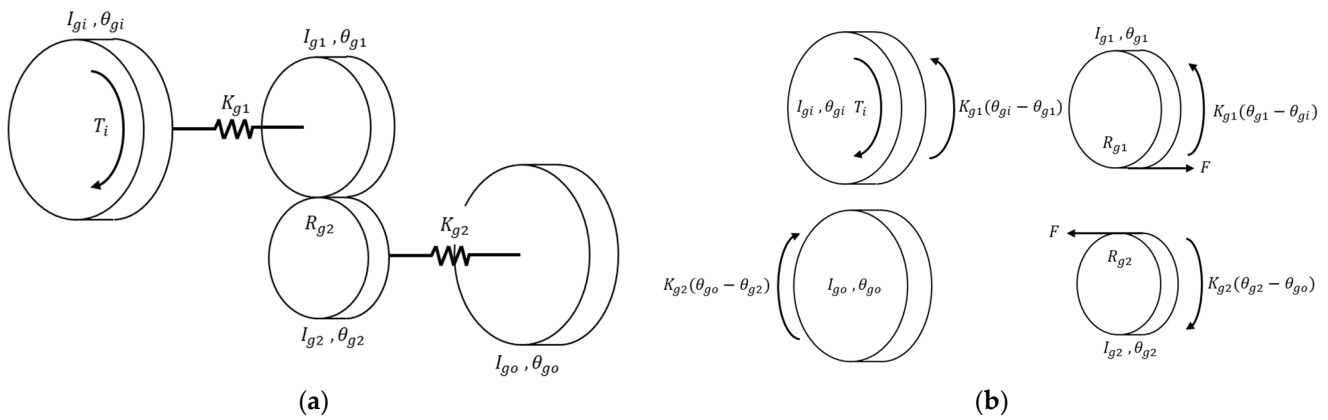


Figure 6. Geared system with 4 DOFs: (a) description of the torsional system with lumped inertias and springs; (b) free body diagram for the equation of motions.

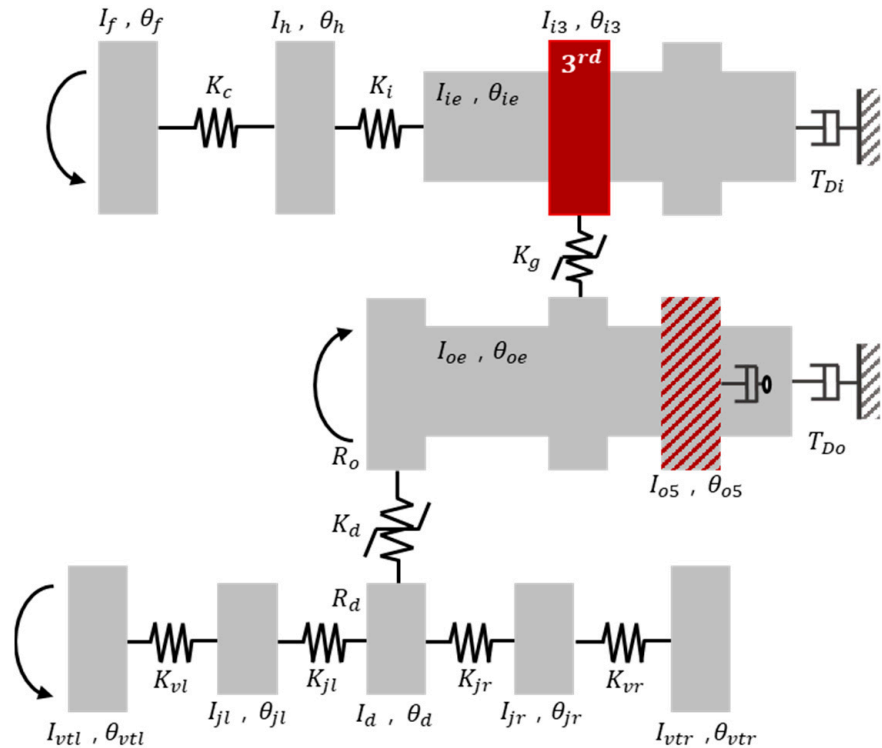


Figure 7. Lumped parameter system model for a 10–DOF torsional system.

To reduce the lumped model for the gear pairs, we can consider a simple geared system, as illustrated in Figure 6. Figure 6 shows a simple geared system with 4 DOFs and its FBD. In this diagram, I_{gi} and I_{go} represent the inertias of input and output gears, respectively, while I_{g1} and I_{g2} show the inertias of speed gear pairs. K_{g1} and K_{g2} present the assumed constant values of the gear mesh stiffness. $\theta_{gi}, \theta_{go}, \theta_{g1}$, and θ_{g2} denote the angular displacements of each lumped mass, as presented in Figure 6. T_i represents the external torque operating on the input gear, and F is the internal force at the contact point between the gear pair. Basic dynamic motions can be derived using the illustrated FBD and Newton's second law, as follows.

$$I_{gi}\ddot{\theta}_{gi} + K_{g1}\theta_{g1} - K_{g1}\theta_{gi} = T_i. \quad (57)$$

$$I_{g1}\ddot{\theta}_{g1} + K_{g1}\theta_{g1} - K_{g1}\theta_{gi} = -(F \times R_{g1}). \quad (58)$$

$$I_{g2}\ddot{\theta}_{g2} + K_{g2}\theta_{g2} - K_{g2}\theta_{go} = (F \times R_{g2}). \quad (59)$$

$$I_{go}\ddot{\theta}_{go} + K_{g2}\theta_{go} - K_{g2}\theta_{g2} = 0. \quad (60)$$

$$\frac{I_{g1}\ddot{\theta}_{g1} + K_{g1}\theta_{g1} - K_{g1}\theta_{gi}}{I_{g2}\ddot{\theta}_{g2} + K_{g2}\theta_{g2} - K_{g2}\theta_{go}} = \frac{-(F \times R_{g1})}{(F \times R_{g2})} = -n. \quad (61)$$

$$(I_{g1} + n^2 I_{g2})\ddot{\theta}_{g1} - K_{g1}\theta_{gi} + (K_{g1} + n^2 K_{g2})\theta_{g1} - nK_{g2}\theta_{go} = 0. \quad (62)$$

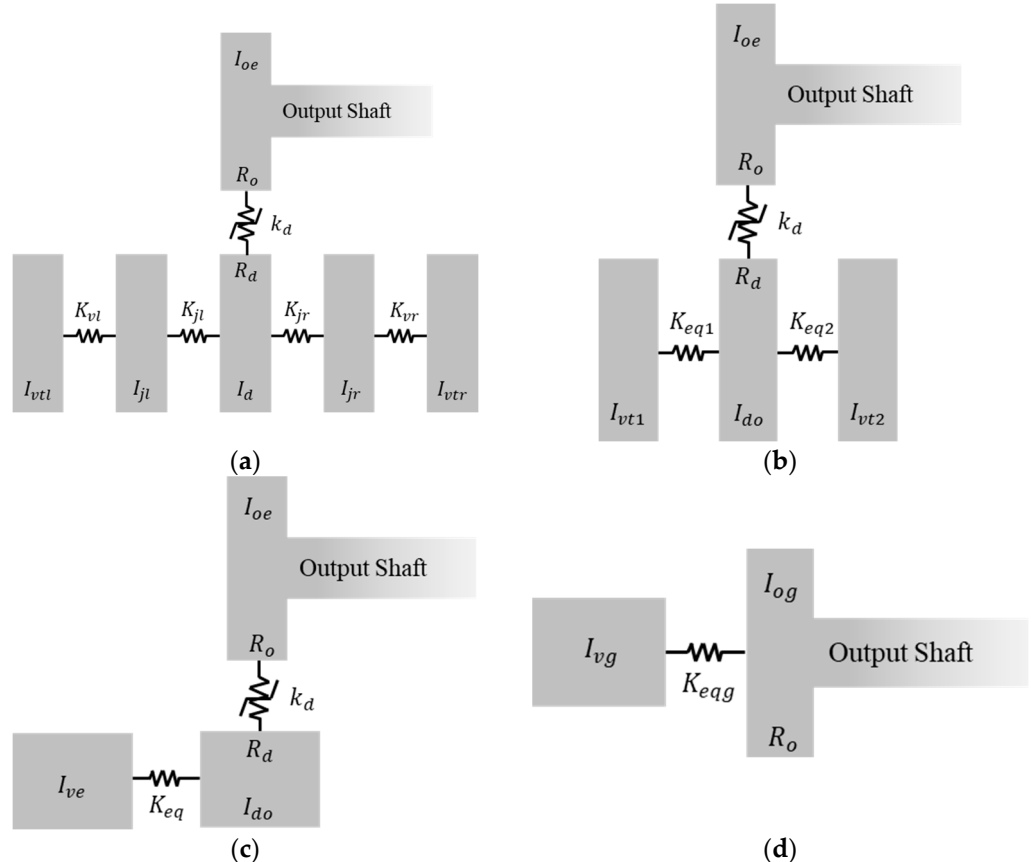


Figure 8. Schematics of the differential gear set: (a) schematic of the final gear drive with 10 DOFs; (b) schematic of the final gear drive with 8 DOFs; (c) schematic of the final gear drive with 7 DOFs; (d) schematic of the final gear drive with 6 DOFs.

Here, Equation (62) is derived from Equations (58) and (59) by utilizing the gear ratio $\frac{R_{g1}}{R_{g2}} = \frac{\dot{\theta}_{g2}}{\dot{\theta}_{g1}} = n$, as described in Equation (61). Consequently, the 4-DOF geared system depicted in Figure 6a is ultimately reduced to a 3-DOF system, in conjunction with Equations (58)–(62). Therefore, using the techniques suggested above, speed gears, such as 1st, 2nd, 4th, and reverse gears, as illustrated in Figure 2, can be combined with the input and output shafts. In summary, the original system with 15 DOFs, as shown in Figure 2, can be reduced to a 10-DOF geared system, as depicted in Figure 7. Thus, the reduced model for the practical system illustrated in Figure 7 is formulated with the reduced DOF using the following basic equations.

$$\underline{\underline{M}}\ddot{\underline{\theta}}(t) + \underline{\underline{K}}\underline{\theta}(t) = \underline{\underline{0}}. \quad (63)$$

$$\underline{\theta} = \left[\theta_f \ \theta_h \ \theta_{ie} \ \theta_{o5} \ \theta_{og} \ \theta_{vg} \right]^T. \quad (64)$$

$$\underline{\underline{M}} = diag \left[I_f, I_h, I_{ie}, I_{o5}, I_{og}, I_{vg} \right]. \quad (65)$$

$$\underline{\underline{K}} = \begin{bmatrix} & \\ & k(i,j) \\ & \end{bmatrix}. \quad (66)$$

$$I_{ie} = I_{ie} + I_{i3} + \left(\frac{R_{i1}}{R_{o1}} \right)^2 I_{o1} + \left(\frac{R_{i2}}{R_{o2}} \right)^2 I_{o2} + \left(\frac{R_{ir}}{R_{ri}} \right)^2 \left\{ I_{ri} + \left(\frac{R_{ri}}{R_{or}} \right)^2 I_{or} \right\}. \quad (67)$$

$$I_{oe} = I_o + \left(\frac{R_{o4}}{R_{i4}} \right)^2 I_{i4}. \quad (68)$$

The inertias of the reduced system were designated as follows: I_{ie} , input shaft lumped with 1st, 2nd, and reverse gears; I_{oe} , output shaft lumped with the 4th gear. In addition, the inertia and stiffness values on the driveshaft could be reduced by assuming equivalent stiffness values for the parallel and series connections of the spring. As illustrated in Figure 8, their equivalent properties were derived as follows.

$$K_{eqg} = (R_o / R_d)^2 K_{eq}, \quad (69a)$$

$$K_{eq} = K_{eq1} + K_{eq2}. \quad (69b)$$

$$K_{eq1} = K_{eq2} = \frac{K_{vr} K_{jr}}{K_{vr} + K_{jr}}. \quad (70)$$

$$I_{vg} = (R_o / R_d)^2 I_{ve}, \quad (71a)$$

$$I_{og} = I_{oe} + (R_o / R_d)^2 I_{do}. \quad (71b)$$

$$I_{ve} = I_{vt1} + I_{vt2}. \quad (72)$$

$$I_{vt1} = I_{vtr} + \frac{I_{jl}}{2}, \quad (73a)$$

$$I_{vt2} = I_{vtr} + \frac{I_{jr}}{2}. \quad (73b)$$

$$I_{do} = I_d + \frac{I_{jl} + I_{jr}}{2}. \quad (74)$$

In Figure 8c, K_{eq} is lumped into K_{eqg} in Figure 8d, as described in Equation (69a). The inertias and stiffnesses employed in the system reduction are designated as follows: I_{do} , differential gear lumped with the left and right cv joints; I_{vt1} , left tire and vehicle lumped with the left cv joint; I_{vt2} , right tire and vehicle lumped with the right cv joint; I_{ve} , whole inertia lumped with I_{vt1} and I_{vt2} ; I_{og} , output shaft lumped with I_{do} ; I_{vg} , inertia of the tire and vehicle affected by the gear ratio (R_o / R_d) ; K_{eq1} , equivalent stiffness of the series connection of K_{vl} and K_{jl} ; K_{eq2} , equivalent stiffness of the series connection of K_{vr} and K_{jr} ; K_{eq} , equivalent stiffness of the parallel connection of K_{eq1} and K_{eq2} ; K_{eqg} , differential stiffness lumped with K_{eq} by employing the gear ratio (R_o / R_d) . Finally, the number of DOFs for the system was

reduced from 10 to 6, as illustrated in Figure 9, and all the components of the stiffness matrix $\underline{\underline{K}}$ from Equation (66) were obtained as follows.

$$K_{1,1} = K_c, \quad (75a)$$

$$K_{2,2} = K_c + K_i. \quad (75b)$$

$$K_{3,3} = K_i + \left(R_{i5}^2 + R_{i3}^2 \right) K_g. \quad (76)$$

$$K_{4,4} = K_g R_{o5}^2. \quad (77)$$

$$K_{5,5} = K_g R_{o3}^2 + K_{eqg}, \quad (78a)$$

$$K_{6,6} = K_{eqg}. \quad (78b)$$

$$k_{1,2} = k_{2,1} = -k_c, \quad (79a)$$

$$k_{2,3} = k_{3,2} = -k_i. \quad (79b)$$

$$k_{3,4} = k_{4,3} = k_g R_{i5} R_{o5}, \quad (80a)$$

$$k_{3,5} = k_{5,3} = k_g R_{i3} R_{o3}. \quad (80b)$$

$$k_{5,6} = k_{6,5} = -k_{eqg}. \quad (81)$$

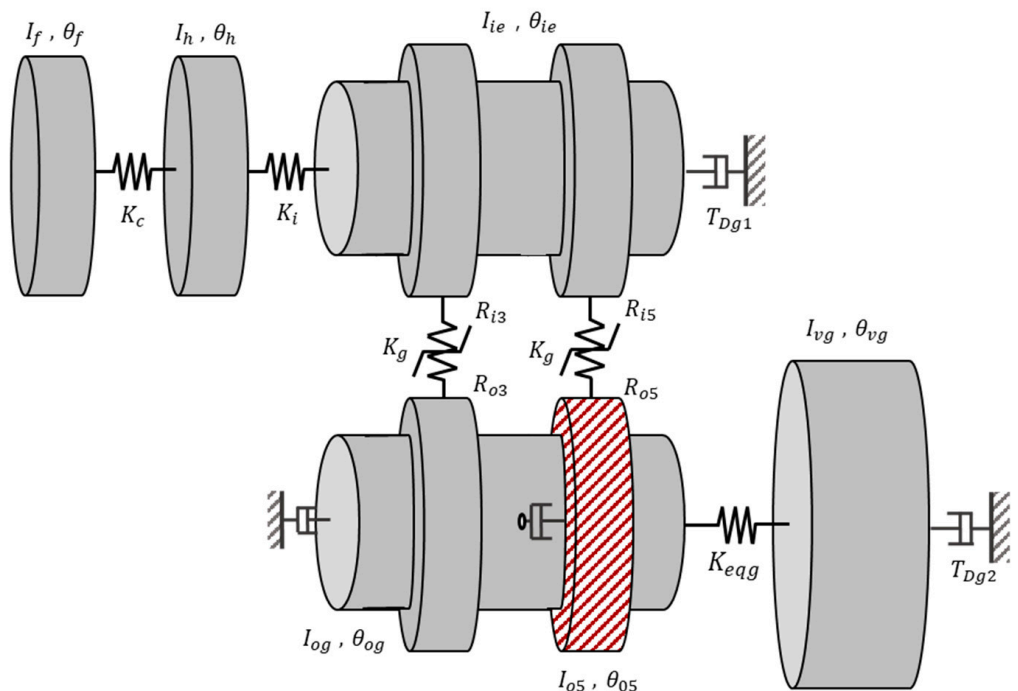


Figure 9. Reduced driveline system model with 6 DOFs based on the original torsional system.

The dynamic characteristics of the 6-DOF system can be obtained using modal analysis. Table 5 and Figure 10 show the first three natural frequencies and mode shapes for both models. Here, the y - and x -axes of Figure 10 are the normalized values of the modal vector and their relevant subsystem, as described in Equations (64) and (65). The differences between the natural frequencies of the 15-DOF and 6-DOF models are due to the reduction effect. The natural frequencies corresponding to the lumped inertia naturally disappeared as the relevant inertia was reduced. Therefore, the 1st natural frequency value of the 15-DOF model did not appear in the 6-DOF model. For example, the 1st mode shown in Figure 4 represents the hopping mode observed in the right and left wheels, which was removed when the differential gear, cv joint, vehicle, and tires were combined during the system reduction. Except for the hopping mode, which was not the main concern of this study, the first three mode shapes and natural frequencies presented in Figure 4, Figure 10 and Table 5 correlated well with each other.

Table 5. First four natural frequencies of the 15- and 6-DOF systems.

Natural Frequency (Hz)	6-DOF	15-DOF
f_1	7.6	2.3
f_2	60.6	7.6
f_3	272.8	60.8
f_4	1846.3	272.5

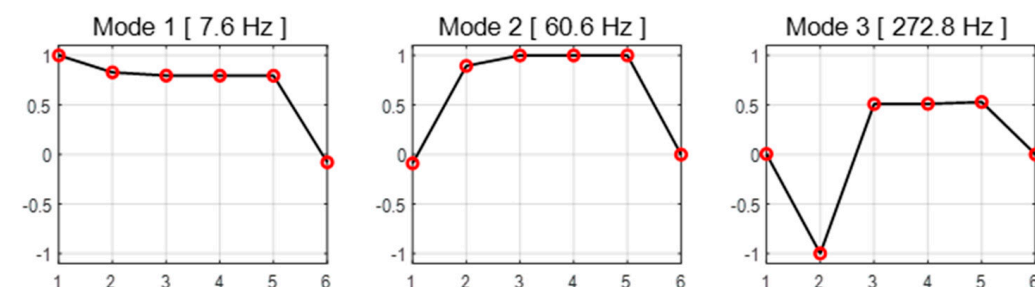


Figure 10. First three modes of the 6-DOF model.

To calculate the frequency response functions, the damping matrix was approximated, and unit torque excitation was considered, as described in Equations (50)–(56). The frequency response functions also correlated well between each model, as compared in Figure 11. The FRFs for both the 15- and 6-DOF system models described in Figure 11 are defined as follows: $|Y_1|$, FRFs of the flywheel; $|Y_2|$, FRFs of the clutch hub; $|Y_3|$, FRFs of the input shaft; $|Y_4|$, FRFs of the 5th gear on the output shaft; $|Y_5|$, FRFs of the output shaft; $|Y_6|$, FRFs of the tire and vehicle. The difference between $|Y_6|$, the FRFs of the vehicle in the 15- and 6-DOF system models, arose during the system reduction process, as the inertia and stiffness values for the vehicle components were modified with respect to the employed gear ratio.

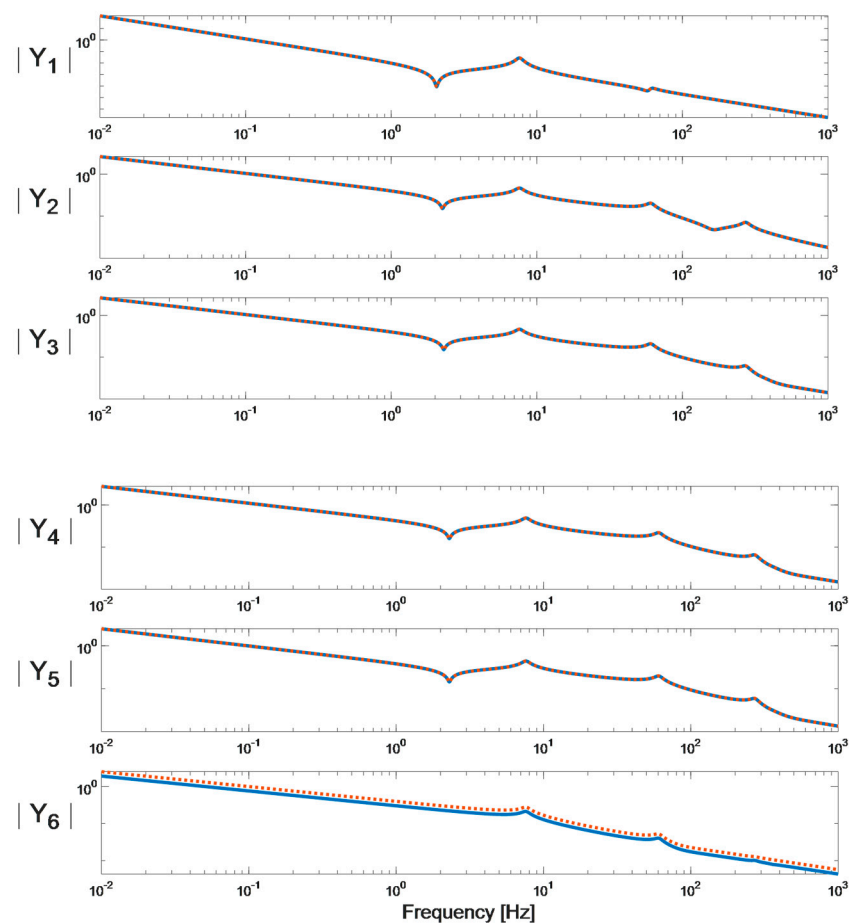


Figure 11. Comparisons of FRFs of 6-DOF model with 15-DOF model. Key: —, 15-DOF; - - -, 6-DOF.

5. Linear Analysis in the Time Domain

From the results based on the modal analysis and FRFs, the linear system responses in the time domain can be investigated to find the main system parameters for improving the noise and vibration conditions. The time domain solutions are obtained with two different approaches. In general, the system responses consist of transient and steady-state terms. First, the basic equation model suggested previously can be used on the basis of the modal analysis and FRFs. For example, the modal domain and FRF results are simply used for investigating the transient and steady-state responses, respectively. Second, the state variable equations can be used as an alternative method which will lead to a simpler calculation procedure than the first approach, since both transient and steady-state responses are obtained simultaneously.

5.1. Time Responses Based on Modal Domain and FRFs

The transient responses can be directly calculated by transferring the modal domain coordinates $\underline{\eta}(t)$ to the physical domain for $\underline{\theta}(t)$, as described in Equation (46). Each coordinate can be estimated along with the initial conditions (ICs) as follows.

$$\underline{\underline{M}} \ddot{\underline{\theta}}(t) + \underline{\underline{C}} \dot{\underline{\theta}}(t) + \underline{\underline{K}} \underline{\theta}(t) = \underline{0}. \quad (82)$$

$$\ddot{\underline{\eta}}(t) + \begin{bmatrix} \ddots & & \\ & 2\zeta w_r & \\ & & \ddots \end{bmatrix} \dot{\underline{\eta}}(t) + \begin{bmatrix} \ddots & & \\ & w_{ri} & \\ & & \ddots \end{bmatrix} \underline{\eta}(t) = \underline{0}. \quad (83)$$

$$\underline{\eta}(t) = e^{-i\omega_{ni}t} [\underline{A}\cos(\omega_{di}t) + \underline{B}\sin(\omega_{di}t)], i = 1, 2, \dots, 6. \quad (84)$$

$$\underline{\eta}(0) = \underline{\phi}^{-1}\underline{\theta}(0), \quad (85a)$$

$$\dot{\underline{\eta}}(0) = \underline{\phi}^{-1}\dot{\underline{\theta}}(0). \quad (85b)$$

The 6-DOF model is a coupled system, as shown in Equation (82). Using the normal modal matrix $\underline{\phi}$ from Equation (45), the coupled system of Equation (82) is transformed into the decoupled system, as derived in Equation (83). Overall, the transient responses of the torsional system can be expressed by Equation (84), where \underline{A} and \underline{B} are arbitrary constant vectors. These unknown constants are determined by substituting the modal initial values $\underline{\eta}(0)$ and $\dot{\underline{\eta}}(0)$. In this study, 0.1 (rad) and 0 (rad/s) were used as the initial torsional displacement and velocity, respectively. Finally, the transient responses of the torsional system in the physical domain were calculated by multiplying $\underline{\phi}$ by $\underline{\eta}(t)$, and the results are shown in Figure 12. Along with the damping effects, the system responses converged to zero well. Here, the transient responses in the physical domain described in Figure 12 are defined as follows: X_{tr1} , transient response for the flywheel; X_{tr2} , transient response for the clutch hub; X_{tr3} , transient response for the input shaft; X_{tr4} , transient response for the 5th gear on the output shaft; X_{tr5} , transient response for the output shaft; X_{tr6} , transient response for the tire and vehicle.

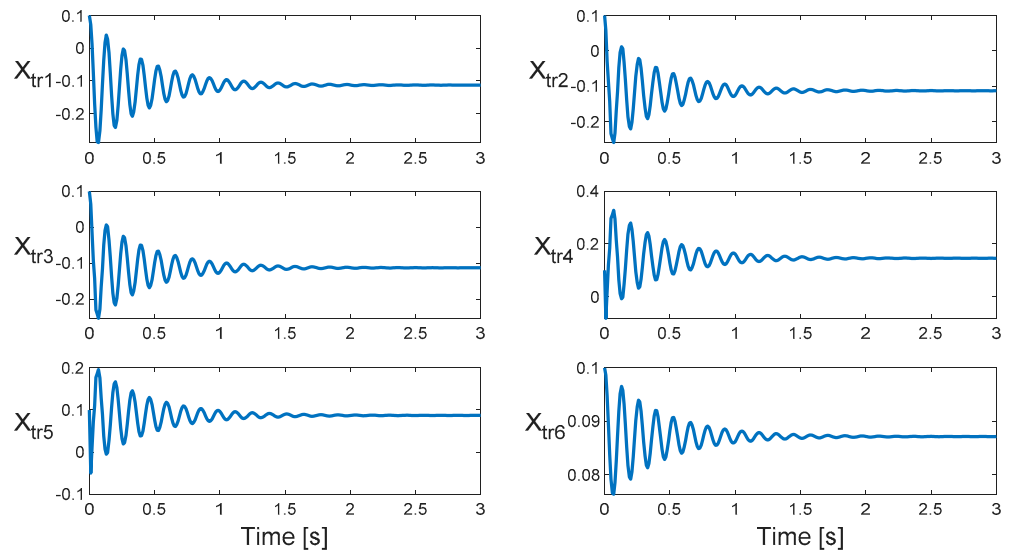


Figure 12. Transient response analysis based on the modal analysis.

From the whole system responses, combined with the transient and steady-state terms, only the steady-state responses are revealed after the transient responses converge to zero completely. To obtain the damped forced responses in a torsional system under sinusoidal excitation, the produced values such as the magnitude and phase from the FRFs, as seen in Figure 11, can be employed. The FRFs for the 6-DOF system can be derived as follows.

$$\underline{\underline{M}}\ddot{\underline{\theta}}(t) + \underline{\underline{C}}\dot{\underline{\theta}}(t) + \underline{\underline{K}}\underline{\theta}(t) = \underline{\underline{T}}(t). \quad (86)$$

$$\underline{\underline{T}}(t) = [1 \ 0 \ 0 \ 0 \ 0 \ 0]^T e^{i\omega t} = \tilde{\underline{\underline{T}}} e^{i\omega t}. \quad (87)$$

$$\underline{\theta}(t) = \tilde{\underline{\theta}} e^{i\omega t}, \quad (88a)$$

$$\tilde{\theta}_n = \left| \tilde{\theta}_n \right| e^{i\varphi_n}, n = 1, 2, \dots, 6. \quad (88b)$$

$$\tilde{\underline{\theta}}(\omega) = \left[\underline{\underline{K}} - \underline{\underline{M}} \cdot \omega^2 + i \cdot \underline{\underline{C}} \cdot \omega \right]^{-1} \tilde{\underline{T}}. \quad (89)$$

$$\underline{\theta}(t) = \left| \tilde{\underline{\theta}}(w_0) \right| e^{i\varphi(w_0)} e^{iw_0 t} \text{ at } w = w_0. \quad (90)$$

The formula for calculating the FRFs in Equation (89) is derived by substituting Equations (88) and (87) into Equation (86). Since the results are generated as a function of frequency ω and are represented as complex values, their magnitudes and phases provide practical information regarding the amplitude and phase shift of the system responses. Thus, the dynamic behaviors in the time domain are obtained as described in Equation (90) for a specific excitation frequency value, ω_0 . To focus on the linear analysis concerning specific noise and vibration problems, such as gear rattle, this study concentrated on the system responses at $\omega_0 = 60$ (Hz). Figure 13 displays the steady-state responses at $\omega_0 = 60$ (Hz) for the torsional system. In Figure 13, the responses from X_{ss1} to X_{ss6} represent, in order: steady-state responses based on the FRF components of the flywheel, clutch hub, input shaft, 5th speed gear on the output shaft, and vehicle.

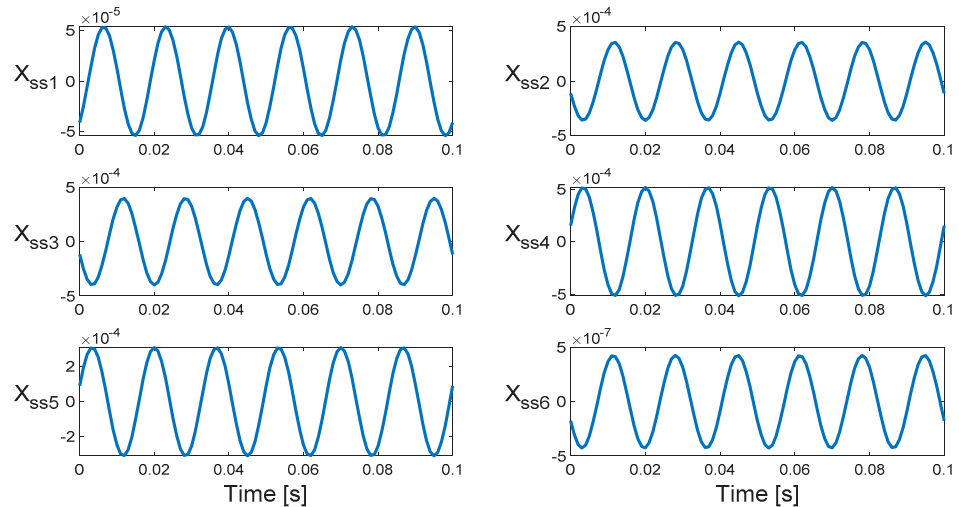


Figure 13. Steady-state responses based on the FRF components.

5.2. Time Responses Based on the State Variable Equation

The equations derived in Equations (82)–(86) are based on the 2nd-order ordinary differential equations (ODE). However, this method using the original forms described in Equations (82)–(86) becomes more complex as the order of the differential equation increases [33]. However, state variables are used to describe the mathematical state of a dynamic system by a set of 1st-order ODEs rather than by one or more nth-order ODEs. Thus, the simulations using the 1st-order ODEs can be more efficient in terms of modeling and analyzing the system responses, especially by including the MIMO (multi-input multi-output) system and time-varying and non-linear effects [25,34]. The state variable equation can be formulated by defining each state variable with the matrix and vector forms, as described in Equations (91) and (92).

$$\dot{\underline{x}}(t) = \underline{\underline{A}} \underline{x}(t) + \underline{\underline{B}} \underline{u}(t). \quad (91)$$

$$\underline{y}(t) = \underline{\underline{C}} \underline{x}(t) + \underline{\underline{D}} \underline{u}(t). \quad (92)$$

Equations (91) and (92) represent the state-space representation. In this representation, $\underline{x}(t)$ is the state vector containing the displacements and velocities, \underline{A} is the system matrix, \underline{B} is the input matrix, \underline{C} is the output matrix, \underline{D} is the constant matrix relevant to the input, $\underline{u}(t)$ is the input vector, and $\underline{y}(t)$ is the concerned output vector. The scope of this study was to investigate the system responses for the torsional dynamic behaviors of the physical system described earlier. Therefore, Equation (92) was not the main focus of this study; instead, Equation (91) was the primary focus for examining the system responses of the torsional system.

5.2.1. Transient Response

The system response in a zero-input case can be calculated using the state transition matrix $\underline{\Phi}(t)$ and the initial values $\underline{x}(0)$. The general process for calculating the transient responses with the state transition matrix, based on the state variable equation, is described as follows [35].

$$\dot{\underline{x}}(t) = \underline{A} \underline{x}(t). \quad (93)$$

$$\underline{x}(t) = \underline{b}_0 + \underline{b}_1 t + \underline{b}_2 t^2 + \underline{b}_3 t^3 + \cdots + \underline{b}_k t^k \cdots. \quad (94)$$

$$\underline{b}_1 + 2\underline{b}_2 t + 3\underline{b}_3 t^2 + \cdots + k\underline{b}_k t^{k-1} \cdots = \underline{A} (\underline{b}_0 + \underline{b}_1 t + \underline{b}_2 t^2 + \underline{b}_3 t^3 + \cdots + \underline{b}_k t^k \cdots). \quad (95)$$

$$\underline{b}_k = \frac{1}{k!} \underline{A}^k \underline{b}_0, \quad (96a)$$

$$\underline{x}(0) = \underline{b}_0. \quad (96b)$$

$$\underline{x}(t) = \sum_{k=0}^{\infty} \frac{\underline{A}^k t^k}{k!} \quad (97a)$$

$$\underline{x}(0) = e^{\underline{A}t} \underline{x}(0). \quad (97b)$$

$$\underline{x}(t) = \underline{\Phi}(t) \underline{x}(0). \quad (98)$$

$$\underline{\Phi}(t) = e^{\underline{A}t} = \underline{u} e^{\underline{\Delta}t} \underline{u}^{-1}. \quad (99)$$

$$e^{\underline{\Delta}t} = \begin{bmatrix} e^{\lambda_1 t} & 0 & 0 & 0 \\ 0 & e^{\lambda_2 t} & 0 & 0 \\ 0 & 0 & \ddots & 0 \\ 0 & 0 & 0 & e^{\lambda_n t} \end{bmatrix}. \quad (100)$$

For this study, the initial values of 0.1 (rad) and 0 (rad/s) were used for the initial torsional displacement $\underline{x}(0)$ and velocity $\dot{\underline{x}}(0)$, respectively. The solution of the system can be assumed on the basis of the power series with arbitrary vectors \underline{b}_0 and \underline{b}_k ($k = 1, 2, 3, \dots$), as described in Equation (94). Thus, substituting Equation (94) into Equation (93) leads to a series expansion as stated in Equation (95). By equating the same t^k terms on both sides of Equation (95), the basic forms of constant vectors \underline{b}_k ($k = 1, 2, 3, \dots$) are expressed as Equation (96), where the initial torsional displacement is represented as $\underline{x}(0) = \underline{b}_0$. Thus, the basic solution of $\underline{x}(t)$ can be written as Equation (97) with the matrix exponential $e^{\underline{A}t}$. Moreover, the matrix exponential $e^{\underline{A}t}$, when the initial conditions are given at $t = 0$ in a linear system, is considered the state transition matrix $\underline{\Phi}(t)$, as described in Equation (98). In addition, $\underline{\Phi}(t)$ can be calculated along with the eigenmatrix \underline{u} and eigenvalue λ_n of the

system matrix $\underline{\underline{A}}$. Figure 14 compares the results of transient responses based on the state variable equation with the ones obtained from the modal analysis, demonstrating a strong correlation between the two.

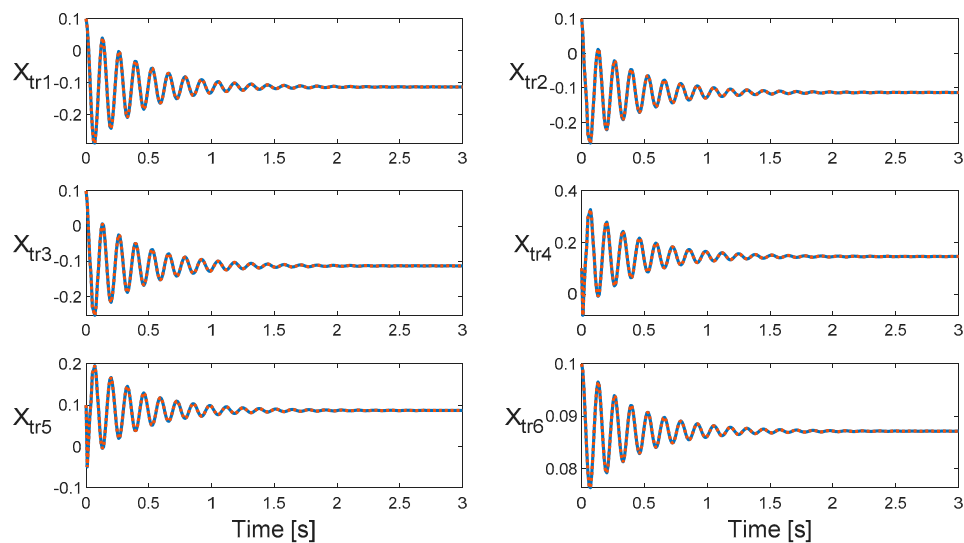


Figure 14. Comparisons of transient responses from two different analyses. Key: —, using the modal analysis; - - -, using the state variable equation.

5.2.2. Steady-State Responses for Semi-Definite System

The steady-state responses using the state variable equation under sinusoidal input can be calculated by employing the state-transition matrix and the convolution method [36,37]. The process of obtaining the steady-state responses using the state transition matrix $\underline{\underline{\Phi}}(t)$ and the initial condition $\underline{x}(0)$ is described as follows.

$$\dot{\underline{x}}(t) - \underline{\underline{A}} \underline{x}(t) = \underline{\underline{B}} \underline{u}(t). \quad (101)$$

$$e^{-\underline{\underline{A}}t} \dot{\underline{x}}(t) - e^{-\underline{\underline{A}}t} \underline{\underline{A}} \underline{x}(t) = e^{-\underline{\underline{A}}t} \underline{\underline{B}} \underline{u}(t). \quad (102)$$

$$\frac{d}{dt} \left\{ e^{-\underline{\underline{A}}t} \underline{x}(t) \right\} = e^{-\underline{\underline{A}}t} \underline{\underline{B}} \underline{u}(t). \quad (103)$$

$$\int_0^t \frac{d}{d\tau} \left\{ e^{-\underline{\underline{A}}\tau} \underline{x}(\tau) \right\} d\tau = \int_0^t e^{-\underline{\underline{A}}\tau} \underline{\underline{B}} \underline{u}(\tau) d\tau. \quad (104)$$

$$e^{-\underline{\underline{A}}t} \underline{x}(t) - \underline{x}(0) = \int_0^t e^{-\underline{\underline{A}}\tau} \underline{\underline{B}} \underline{u}(\tau) d\tau. \quad (105)$$

$$\underline{x}(t) = e^{\underline{\underline{A}}t} \underline{x}(0) + \int_0^t e^{\underline{\underline{A}}(t-\tau)} \underline{\underline{B}} \underline{u}(\tau) d\tau. \quad (106)$$

Here, the same initial condition, $\underline{x}(0)$, that was used for the transient responses was employed to calculate the steady-state responses. In addition, Equation (101) represents a revised formula achieved by transferring the term $\underline{\underline{A}} \underline{x}(t)$ to the left side of Equation (91), resulting in Equation (102) by multiplying $e^{-\underline{\underline{A}}t}$ on both sides of Equation (101). Furthermore, the left side of Equation (102) reflects the partial derivative of $e^{-\underline{\underline{A}}t} \underline{x}(t)$, which is summarized as Equation (103). Integrating both sides of Equation (103) over the range from 0 to t yields Equations (104)–(106). Using these final-form equations to calculate the steady-state responses, the dynamic behaviors of the system are shown in Figure 15. When comparing the results based on the FRF method and state variable equations, it is evident that they are well correlated for X_{ss2} , X_{ss3} , X_{ss4} , and X_{ss5} , as clearly seen in Figure 15. However, the

simulated results for X_{ss1} and X_{ss6} exhibit significant discrepancies between the FRFs and state variable equation methods, primarily due to the rigid body mode observed at 0 Hz for the semi-definite system. This mode can lead to numerical issues that might mislead the integration routine by introducing an arbitrary constant, including infinity, into all solutions [12]. Thus, to thoroughly investigate the dynamic responses occurring between each coupled system, the absolute motions must be transformed into relative coordinates, thereby converting the semi-definite configuration into the definite system model [25].

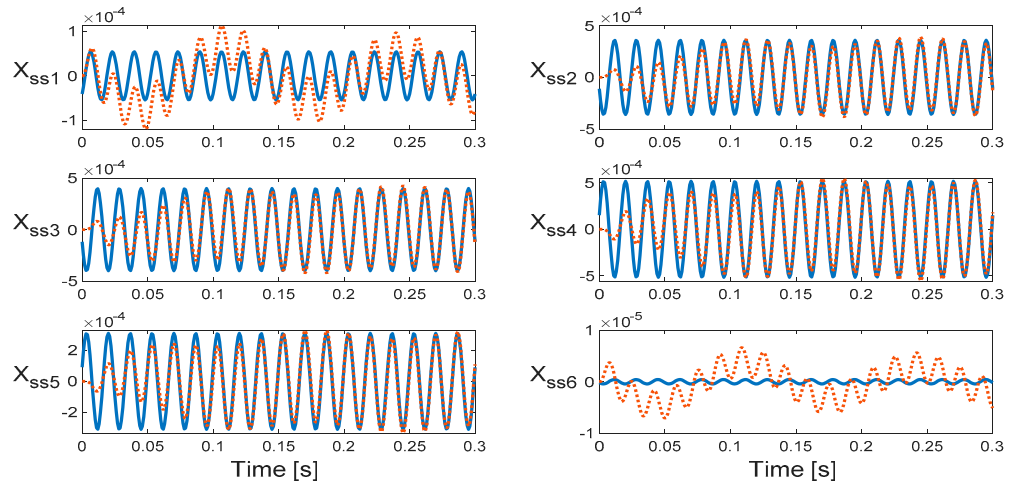


Figure 15. Examination of steady-state responses with absolute motions. Key: —, using the FRFs; - - -, using the state variable equation.

To transform the semi-definite system into a positive-definite system, new coordinates can be defined as $q_1 = \theta_f - \theta_h$, $q_2 = \theta_h - \theta_{ie}$, $q_3 = R_{i5}\theta_{ie} + R_{o5}\theta_{o5}$, $q_4 = R_{i3}\theta_{ie} + R_{o3}\theta_{og}$, and $q_5 = \theta_{og} - \theta_{vg}$. Thus, the relative angular displacement vector \underline{q} and linear transformation matrix $\underline{\underline{P}}$ can be expressed as follows [12].

$$\underline{q} = \begin{bmatrix} q_1 \\ q_2 \\ q_3 \\ q_4 \\ q_5 \end{bmatrix} = \begin{bmatrix} 1 & -1 & 0 & 0 & 0 \\ 0 & 1 & -1 & 0 & 0 \\ 0 & 0 & R_{i5} & R_{o5} & 0 \\ 0 & 0 & R_{i3} & 0 & R_{o3} \\ 0 & 0 & 0 & 0 & 1 \end{bmatrix} \begin{bmatrix} \theta_f \\ \theta_h \\ \theta_{ie} \\ \theta_{o5} \\ \theta_{og} \\ \theta_{vg} \end{bmatrix} = \underline{\underline{P}} \underline{\theta}. \quad (107)$$

$$\underline{\underline{M}}^* \ddot{\underline{q}}(t) + \underline{\underline{C}}^* \dot{\underline{q}}(t) + \underline{\underline{K}}^* \underline{q}(t) = \underline{T}^*(t). \quad (108)$$

$$\underline{\underline{M}}^* = \underline{\underline{P}} \underline{\underline{M}}^{-1} \underline{\underline{M}} \underline{\underline{P}}^*, \quad (109a)$$

$$\underline{\underline{C}}^* = \underline{\underline{P}} \underline{\underline{M}}^{-1} \underline{\underline{C}} \underline{\underline{P}}^*. \quad (109b)$$

$$\underline{\underline{K}}^* = \underline{\underline{P}} \underline{\underline{M}}^{-1} \underline{\underline{K}} \underline{\underline{P}}^*, \quad (110a)$$

$$\underline{T}^*(t) = \underline{\underline{P}} \underline{\underline{M}}^{-1} \underline{T}(t). \quad (110b)$$

$$\underline{\underline{P}}^* = \underline{\underline{P}}^t (\underline{\underline{P}} \underline{\underline{P}}^t)^{-1}, \quad (111a)$$

$$\underline{\underline{P}} \underline{\underline{P}}^t (\underline{\underline{P}} \underline{\underline{P}}^t)^{-1} = \underline{\underline{I}}. \quad (111b)$$

$$\dot{\underline{x}}(t) = \underline{\underline{A}}^* \underline{x}(t) + \underline{\underline{B}}^* \underline{u}^*(t). \quad (112)$$

$$\underline{x}(t) = [q_1 \ q_2 \ q_3 \ q_4 \ q_5 \ \dot{q}_1 \ \dot{q}_2 \ \dot{q}_3 \ \dot{q}_4 \ \dot{q}_5]^T, \quad (113a)$$

$$\underline{\underline{A}}^* = \begin{bmatrix} 0 & I \\ -\frac{\underline{\underline{K}}^*}{\underline{\underline{M}}^*} & -\frac{\underline{\underline{C}}^*}{\underline{\underline{M}}^*} \end{bmatrix}. \quad (113b)$$

$$\underline{\underline{B}}^* = 0, \quad \underline{\underline{B}}^*(6,1) = 1, \quad (114a)$$

$$\underline{u}^*(t) = \underline{\underline{P}} \underline{\underline{M}}^{-1} \underline{u}(t). \quad (114b)$$

From Equations (107)–(114), $\underline{\underline{P}}$ is not generated as a square matrix. Therefore, to determine the inverse matrix with respect to $\underline{\underline{P}}$, the product of $\underline{\underline{P}}$ and $\underline{\underline{P}}^t$ can be introduced, as indicated in Equation (111b), where $\underline{\underline{P}}^* = \underline{\underline{P}}^t (\underline{\underline{P}} \underline{\underline{P}}^t)^{-1}$ of Equation (111a) is defined as a pseudo-inverse matrix. Overall, Equation (108) has new coordinates transferred from the absolute displacement $\theta(t)$ to the relative displacement $\underline{q}(t)$, resulting in a positive-definite system. Using Equations (107)–(111), the state variable equation can be derived as expressed in Equations (112)–(114). In these equations, $\underline{x}(t)$, $\underline{\underline{A}}^*$, $\underline{\underline{B}}^*$, and $\underline{u}^*(t)$ represent state variables, the system matrix, input matrix, and input vector related to the system parameters based on $\underline{\underline{M}}^*$, $\underline{\underline{C}}^*$ and $\underline{\underline{K}}^*$. The steady-state responses with the new coordinate systems, based on Equations (107)–(114), are presented in Figure 16 and compared with the time responses based on FRFs. From the comparisons between two sets of results based on the state variable model and FRFs, it is evident that they are well correlated with each other. Furthermore, the rigid body modes within the nearly zero frequency ranges are completely eliminated.

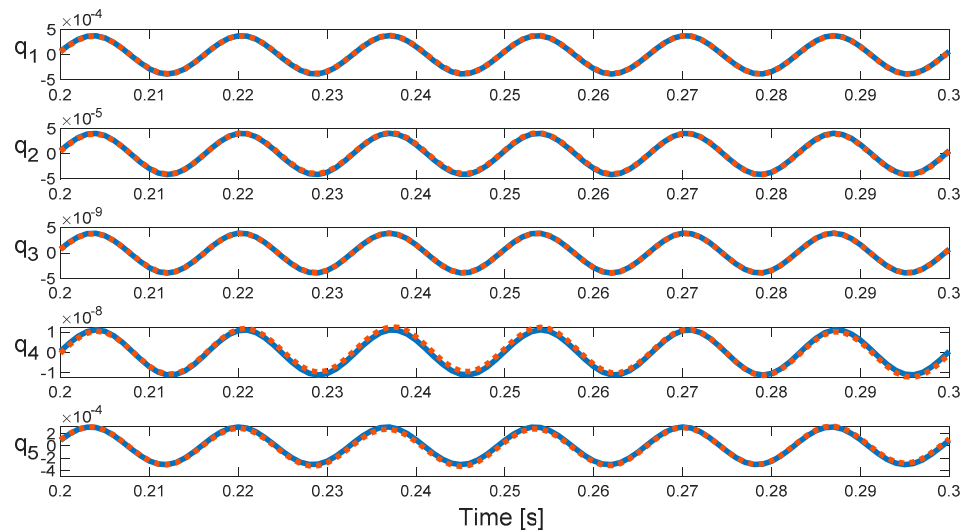


Figure 16. Steady-state responses based on the relative motions. Key: —, using the FRFs; - - -, using the state variable equation.

6. Case Study

Dynamic characteristics in a geared system can be investigated by focusing on several key parameters such as clutch stiffness K_c , unloaded gear inertia I_{05} , and gear mesh stiffness K_g with respect to torsional vibration problems such as gear rattle and whine. To investigate the effects of these key parameters for resolving the aforementioned issues, the relevant parameters, such as K_c , I_{05} , and K_g , were examined [1,5–8,14,20,22,38–40]. For example, to

improve gear rattle conditions, prior research has suggested modifying clutch stiffness K_c and unloaded gear inertia I_{05} [1,5–8,14]. On the other hand, gear whine is closely related to gear properties such as the gear involute and mesh stiffness. In general, K_c consists of multi-staged clutch dampers, as illustrated in Figure 17. Figure 17a illustrates the physical drawing of the entire clutch system with the clutch damper indicated as the clutch spring. Typically, multi-clutch spring components are located inside the clutch housing along with the clutch friction disk. Figure 17b presents an example of the clutch stiffness profile, featuring two staged clutch springs or clutch dampers [1]. In addition, K_g exhibits nonlinear dynamic characteristics along with gear rotational motions under the symmetric condition, as depicted in Figure 18. However, for the purposes of linear analysis concerning the effects of key parameters such as K_c , I_{05} , and K_g , this study employed various constant values to investigate their relationship with primary torsional vibratory problems, namely gear rattle and whine.

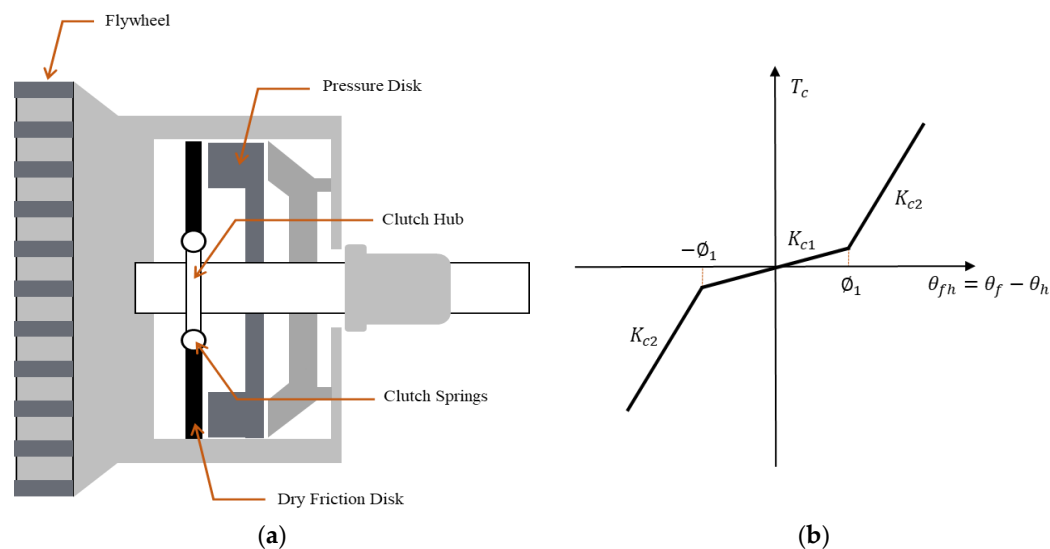


Figure 17. Clutch stiffness K_c : (a) schematic of clutch; (b) clutch torque induced by stiffness [1].

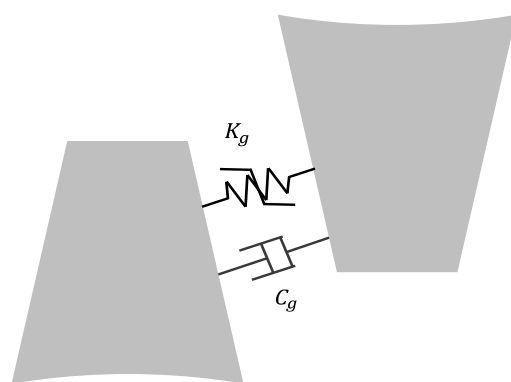


Figure 18. Gear mesh stiffness K_g .

6.1. Case Study I: Clutch Stiffness K_c

The natural frequencies of the system are compared for three different clutch stiffness values, as summarized in Table 6, where the values of K_{c1} and K_{c2} are given as $595.8 \text{ N}\cdot\text{m}\cdot\text{rad}^{-1}$ and $(K_{c1} + K_c)/2$, respectively. Significant changes were observed in the second natural frequency because the dynamic behavior at the second mode was mostly affected by clutch stiffness. This effect was clearly observed in the mode shapes presented in Figures 3, 9 and 18a. When examining the second mode shapes (clutch spring modes) with various K_c values, as seen in Figure 19a, their basic mode shapes were nearly identical,

except for the calculated natural frequencies, which are compared in Tables 6 and 7. In general, gear rattle was closely related to this clutch spring mode, which operates within the second resonance region [1,8,14]. Thus, based on the linearly simulated results presented in Figure 19a and Tables 6 and 7, clutch stiffness can be considered a key parameter for resolving gear impact problems.

Table 6. Comparison of natural frequencies along with clutch stiffnesses for the positive definite system.

Natural Frequency (Hz)	K_{c1} (595.8 N·m·rad ⁻¹)	K_{c2} (1216.9 N·m·rad ⁻¹)	Original K_c (1838 N·m·rad ⁻¹)
f_1	6.6	7.3	7.6
f_2	40.6	51.8	60.6
f_3	266.0	269.4	272.8
f_4	1845.7	1845.7	1846.3
f_5	4484.9	4484.9	4485.7

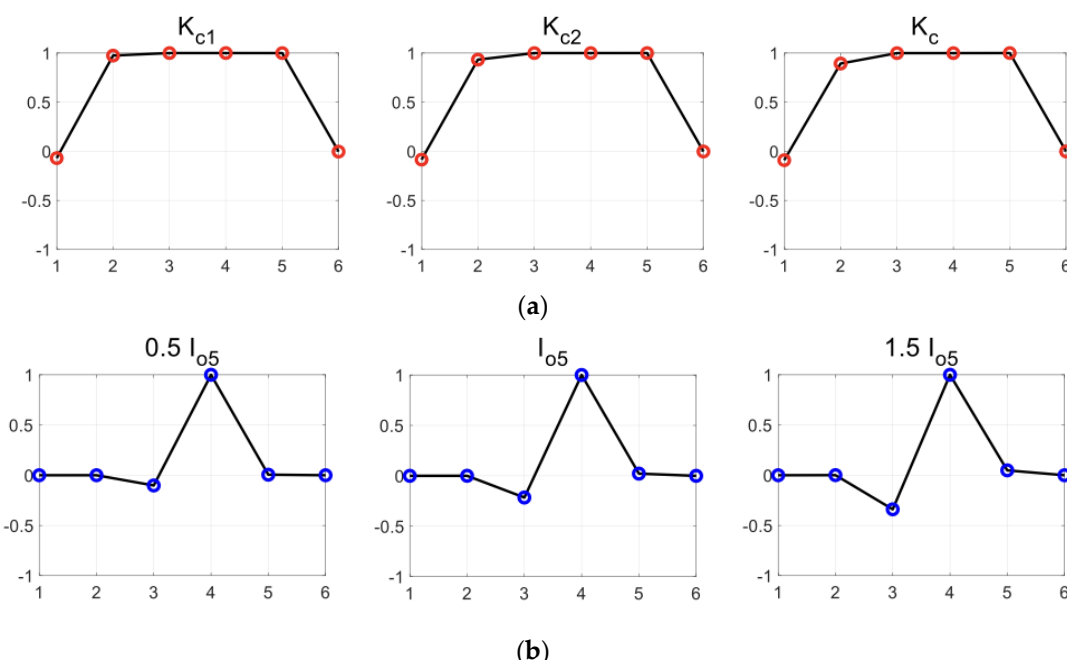


Figure 19. Mode shapes along with K_c and I_{o5} values: (a) second mode shapes with various K_c ; (b) fifth mode shapes with various I_{o5} .

Table 7. Components of second modal vectors along with various K_c values.

2nd Mode Shape	K_{c1}	K_{c2}	K_c
1. flywheel	-0.0693	-0.0847	-0.0903
2. clutch hub	0.9742	0.9328	0.8930
3. input shaft	0.9999	0.9997	0.9992
4. unloaded gear	1	0.9999	0.9994
5. output shaft	0.9996	1	1
6. vehicle + wheel	-0.0032	-0.0020	-0.0014

The effect of K_c was also evident from the time domain analysis, as shown in Figure 20. To investigate the time domain responses, the relative motions in terms of $q_3(t)$ and $q_4(t)$ were the primary focus, as gear impacts and their associated torsional vibrations generally occur at the gear pairs. To simulate the system responses in the time domain, the engine torque T_e was employed as the excitation torque, as described below.

$$T_e = T_m + T_{pm} \cos(w_p t) \quad (115)$$

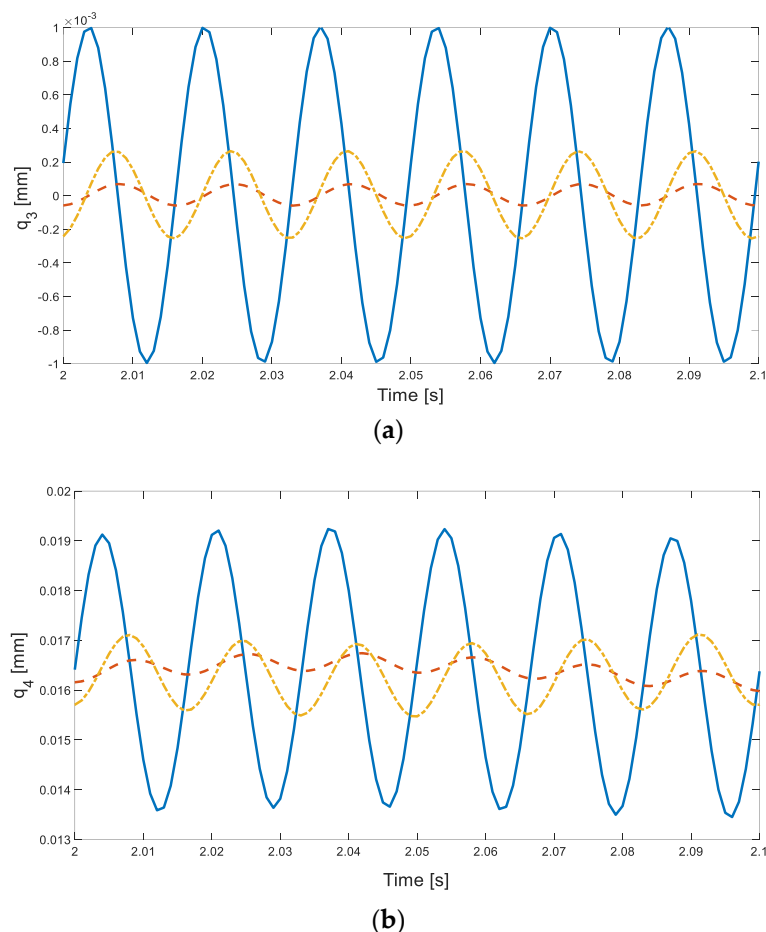


Figure 20. Comparisons of steady-state responses along with K_c values for the positive-definite system: (a) steady-state responses of q_3 ; (b) steady-state responses of q_4 . Key: —, K_{c1} ; —, K_c ; - - -, K_{c2} .

Here, T_m and T_{pm} represent the mean and alternating components of the engine torque, respectively, and w_p is the firing frequency, with the values used for T_m , T_{pm} , and w_p being 168.9 N·m, 251.5 N·m, and 60 Hz, respectively [1]. Figure 20 compares the time responses for q_3 and q_4 , which represent the relative motions between unloaded and loaded gear pairs, respectively. Figure 20a illustrates the system responses with various K_c values. It is worth noting that the amplitude of q_3 decreased as the value of K_c was reduced. For instance, when smaller values such as K_{c1} ($595.8 \text{ N}\cdot\text{m}\cdot\text{rad}^{-1}$) and K_{c2} ($1216.9 \text{ N}\cdot\text{m}\cdot\text{rad}^{-1}$) were employed, the amplitude of q_3 decreased compared with the response for K_c ($1838 \text{ N}\cdot\text{m}\cdot\text{rad}^{-1}$). This reduction in amplitude was further confirmed when comparing the peak-to-peak values, as summarized in Table 8. Furthermore, Figure 20b and Table 8 demonstrate that q_4 was also significantly influenced by the key parameter K_c . In this context, q_3 can be expected to reflect the gear rattle status, which occurs at the unloaded gear pair. In addition, q_4 can be considered the vibratory conditions transferred from the loaded gear pair to the rest parts of the driveline. Consequently, these results provide valuable insights into improving the vibration conditions associated with gear rattle, as compared in Figure 20 and Tables 6–8, even though they do not explicitly depict the gear contact motions. In summary, it can be concluded that clutch stiffness values have a significant influence on the dynamic behavior of the gears, and reducing clutch stiffness improves the vibrational problems caused by gear impacts.

Table 8. Comparison of peak-to-peak value along with various K_c values.

	Peak-to-Peak Value q_3 (mm)	Peak-to-Peak Value q_4 (mm)
K_{c1} (595.8 N·m·rad $^{-1}$)	1.2723×10^{-4}	3.9210×10^{-4}
K_{c2} (1216.9 N·m·rad $^{-1}$)	5.1967×10^{-4}	15×10^{-4}
Original K_c (1838 N·m·rad $^{-1}$)	20×10^{-4}	56×10^{-4}

6.2. Case Study II: Unloaded Gear Inertia I_{o5}

Once again, the natural frequencies of the system, along with the unloaded gear inertia I_{o5} , are listed in Table 9. In this case, $0.5I_{o5}$ (1.30×10^{-4} kg·m 2) and $1.5I_{o5}$ (3.92×10^{-4} kg·m 2) were used for comparison with the original I_{o5} . With different values for I_{o5} , only the natural frequency f_5 , as shown in Table 9, was affected, while the other natural frequencies remained nearly the same. For instance, when I_{o5} varied, natural frequencies f_1 , f_2 , f_3 , and f_4 showed minimal variation. However, the natural frequency f_5 exhibited a clear change, with an increase (or decrease) in I_{o5} resulting in higher (or lower) values, such as 6040.3 (or 3845.5) Hz compared with the original value of 4485.7 Hz.

Table 9. Comparison of natural frequencies along with inertia values of the unloaded gear for the positive-definite system.

Natural Frequency (Hz)	$0.5 I_{o5}$	Original I_{o5} (5.23×10^{-4})	$1.5 I_{o5}$
f_1	7.6	7.6	7.6
f_2	61.5	60.6	59.8
f_3	274.7	272.8	271.1
f_4	1897.0	1846.3	1795.8
f_5	6040.3	4485.7	3845.5

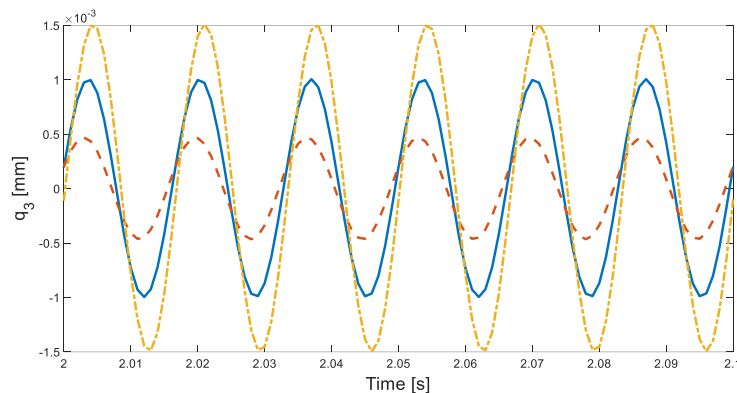
This effect of I_{o5} is evident in Figure 19b, Tables 10 and 11. Upon examining the mode shapes, it becomes apparent that only the fifth mode shape, corresponding to natural frequency f_5 , was significantly influenced by I_{o5} compared with the other sub-systems, as shown in Table 11. Furthermore, the comparison between Tables 10 and 11 reveals that the mode shape was primarily affected at the fifth mode, except for the second mode, providing valuable insights into the relationship between unloaded gear inertia and gear dynamic motions for various I_{o5} values. Figure 21 displays the steady-state responses of q_3 and q_4 for the unloaded and loaded gear pairs, respectively, with $0.5I_{o5}$, $1.5I_{o5}$, and the original I_{o5} . As observed from the modal analysis regarding the effect of I_{o5} mentioned earlier, the steady-state responses of q_3 in the time domain also exhibited significant changes with different I_{o5} values, as depicted in Figure 21a.

Table 10. Components of second modal vectors along with various I_{o5} values.

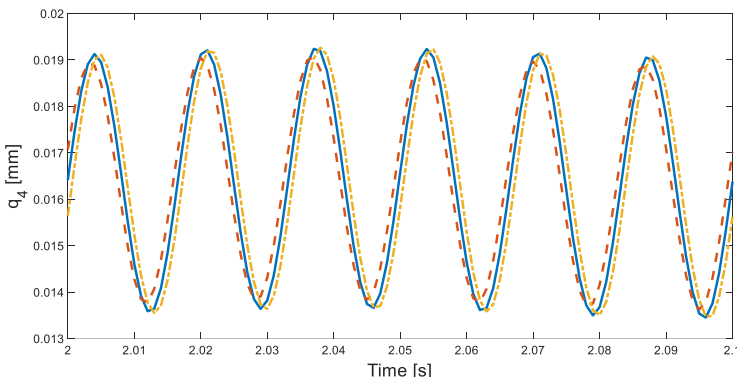
Second Mode Shape	$0.5 I_{o5}$	I_{o5}	$1.5 I_{o5}$
1. flywheel	−0.0878	−0.0903	−0.0929
2. clutch hub	0.9853	0.8930	0.8908
3. input shaft	0.9991	0.9992	0.9992
4. unloaded gear	0.9992	0.9994	0.9996
5. output shaft	1	1	1
6. vehicle + wheel	−0.0014	−0.0014	−0.0015

Table 11. Components of fifth modal vectors along with various I_{05} values.

Fifth Mode Shape	$0.5 I_{05}$	I_{05}	$1.5 I_{05}$
1. flywheel	0	0	0
2. clutch hub	0.0001	0.0005	0.0010
3. input shaft	-0.1018	-0.2150	-0.3392
4. unloaded gear	1	1	1
5. output shaft	0.0055	0.0218	0.0487
6. vehicle + wheel	0	0	0



(a)



(b)

Figure 21. Comparisons of steady-state responses along with I_{05} values for the positive-definite system: (a) steady-state responses of q_3 ; (b) steady-state responses of q_4 . Key: ■■■■, $0.5 I_{05}$; —, $1 I_{05}$; - - -, $1.5 I_{05}$.

For example, a reduction (or increase) in the inertia value of I_{05} led to a corresponding reduction (or increase) in the amplitude of response. This was also evident when compared to the peak-to-peak values summarized in Table 12. On the other hand, q_4 , associated with the loaded gear pair, demonstrated minimal variation across different I_{05} values, as evident in Figure 21b and Table 12. These results underline the importance of I_{05} in addressing gear rattle issues, even in the context of linear analysis. Generally, reducing the inertia of the unloaded gear aligns with prior studies' findings as an effective approach to improving gear rattling conditions [8]. In summary, it can be concluded that unloaded gears also have a significant influence on specific dynamic behaviors such as gear rattle. Therefore, altering the inertia values of unloaded gears relevant to the gear impact problems can improve the gear impact conditions when designing the clutch stiffness.

Table 12. Comparison of peak-to-peak value along with unloaded gear I_{o5} values.

	Peak-to-Peak Value q_3 (mm)	Peak-to-Peak Value q_4 (mm)
$0.5 I_{o5}$	9.2703×10^{-4}	52×10^{-4}
I_{o5}	20×10^{-4}	56×10^{-4}
$1.5 I_{o5}$	30×10^{-4}	56×10^{-4}

6.3. Case Study III: Gear Mesh Stiffness K_g

Table 13 presents a comparison of natural frequencies for various K_g values. Upon examining the calculated natural frequencies, it becomes evident that there were no discernible differences below 300 Hz. However, in the higher frequency range, above 300 Hz, substantial differences emerged, as illustrated in Table 13. Notably, the natural frequencies, associated with dominant gear dynamic modes were significantly influenced by variations in $0.1 K_g$ ($2.7 \times 10^7 \text{ N}\cdot\text{m}^{-1}$), K_g , and $10 K_g$ ($2.7 \times 10^9 \text{ N}\cdot\text{m}^{-1}$). Here, the natural frequencies corresponding to f_4 and f_5 exhibited pronounced changes, with f_4 and f_5 decreasing (or increasing) as K_g decreased (or increased).

Table 13. Comparison of natural frequencies along with gear mesh stiffnesses K_g for the positive-definite system.

Natural Frequency (Hz)	$0.1 K_g$	Original K_g (2.7×10^8)	$10 K_g$
f_1	7.6	7.6	7.6
f_2	60.6	60.6	60.6
f_3	264.5	272.8	273.5
f_4	603.5	1846.3	5820
f_5	1422.1	4485.7	14,170

Despite these variations in natural frequencies, the mode shapes for fourth and fifth modes remained nearly identical, as clearly shown in Figure 22, Tables 14 and 15. While the modal vectors themselves did not exhibit differences with various K_g , the mode shapes for both the fourth and fifth modes suggest that gear dynamic motions were indeed dominant, as evident in Figure 22. The fourth mode shapes depicted in Figure 22a indicate that both the unloaded and loaded gear pairs contributed significantly to the dominant motions. On the other hand, the fifth mode was influenced more by the unloaded gear pairs, as observed in Figure 22b. Overall, both the fourth and fifth modes are expected to play a crucial role in gear dynamic behaviors.

Table 14. Components of fourth modal vectors along with various K_g .

4th Mode Shape	$0.1 K_g$	K_g	$10 K_g$
1. flywheel	0.0001	0	0
2. clutch hub	-0.1100	-0.0104	-0.0010
3. input shaft	0.7801	0.7942	0.7954
4. unloaded gear	1	1	1
5. output shaft	-0.8204	-0.9503	-0.9625
6. vehicle + wheel	0	0	0

Table 15. Components of fifth modal vectors along with various K_g .

5th Mode Shape	$0.1 K_g$	K_g	$10 K_g$
1. flywheel	0	0	0
2. clutch hub	0.0049	0.0005	0
3. input shaft	-0.2212	-0.2150	-0.2144
4. unloaded gear	1	1	1
5. output shaft	0.0224	0.0218	0.0218
6. vehicle + wheel	0	0	0

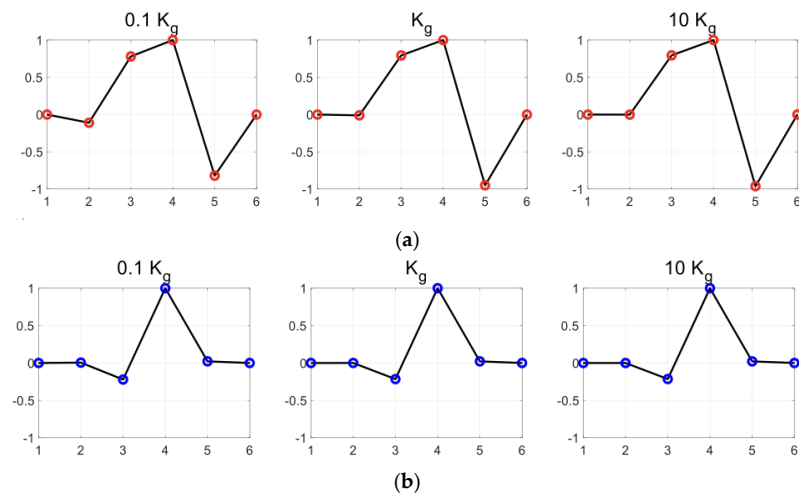


Figure 22. Mode shapes according to different K_g : (a) fourth mode shapes; (b) fifth mode shapes.

Figure 23 presents comparisons of steady-state responses in the time domain, occurring at the unloaded and loaded gear pairs. When evaluating q_3 along with different K_g values, it becomes apparent that the amplitudes of steady-state responses decreased as K_g increased, as shown in Figure 23a. These significant changes are further corroborated by the peak-to-peak values, as detailed in Table 16. Similarly, when comparing the time responses of the loaded gear pair, the same influences observed in the unloaded gear pair were evident, as depicted in Figure 23b and Table 16. Moreover, the mean values of time responses for the loaded gear pair were significantly affected. Specifically, as K_g increased, the mean values of steady-state responses approached zero. These results underline the impact of K_g on gear dynamic motions, particularly noticeable in the case of the loaded gear pairs, which are central to issues such as gear whine vibrations [38–40].

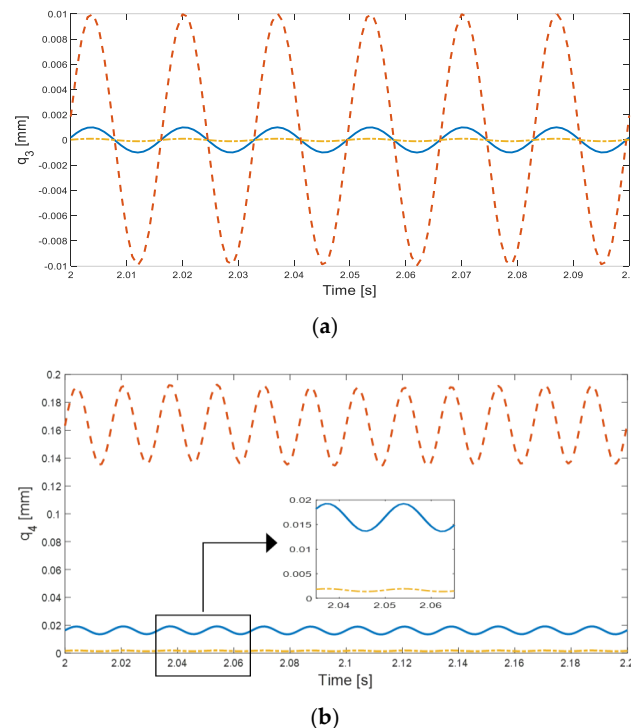


Figure 23. Comparisons steady-state responses along with K_g values using the positive definite system: (a) third steady-state responses based relative motion q_3 ; (b) fourth steady-state responses based relative motion q_4 . Key: ■■■■■, $0.1 K_g$; —, $1 K_g$; - - - -, $10 K_g$.

Table 16. Comparison of peak-to-peak value along with various K_g values.

	Peak-to-Peak Value q_3 (mm)	Peak-to-Peak Value q_4 (mm)
$0.1 K_g$	199×10^{-4}	567×10^{-4}
$1 K_g$	20×10^{-4}	56×10^{-4}
$10 K_g$	1.9951×10^{-4}	5.5771×10^{-4}

In summary, it can be concluded that mesh stiffness significantly influences other specific gear dynamic behaviors, such as gear whine, which can occur in both loaded and unloaded gear pairs. Therefore, designing appropriate mesh stiffness values contributes to improving gear parametric excitations.

7. Conclusions

This study investigated the vehicle driveline under symmetric conditions using a linear analytical method to explore the dynamic characteristics of a specific manual transmission with a front-engine/front-wheel configuration. To examine these dynamics, a mathematical model based on a practical powertrain assembly was developed. The contributions of this study can be summarized as follows. First, a mathematical technique to reduce the number of DOFs for simulation was proposed, and its validity was established. Consequently, the dynamic characteristics, including eigensolutions and frequency response functions (FRFs) of the reduced system model, demonstrated a strong correlation with the simulated results of the original model. Second, this study extensively investigated a linear analysis model based on state variable equations. The linear results derived from the state variable equations were successfully validated against those from the FRF method. Furthermore, the findings based on the state variable equations effectively captured the relationships between key parameters and their associated vibratory issues, such as gear rattle and whine problems. Thus, this study successfully proposed the utilization of linear analytical methods to investigate and determine gear impact and excitation problems and their relevant key parameters in order to simplify the analysis compared to the complexity of nonlinear analysis.

The present study primarily emphasized the linear analytical method, specifically concentrating on the state variable equations, which can serve as the foundation for nonlinear analysis, incorporating features such as gear contact models. However, the current study has limitations in capturing the actual nonlinear dynamic behaviors, such as gear impact and gear time-varying motions. Therefore, the next stage of this research will implement a more advanced analytical model utilizing state variable forms while incorporating nonlinear properties, such as gear backlash and multi-staged clutch dampers.

Author Contributions: J.-M.B., S.-H.K. and J.-Y.Y. initiated and developed the ideas related to this research work. J.-M.B. and S.-H.K. developed parametric studies, analyzed relevant cases, and carried out performance analyses and numerical analyses. J.-M.B. wrote the paper draft under J.-Y.Y.'s guidance, and J.-Y.Y. finalized the paper. All authors have read and agreed to the published version of the manuscript.

Funding: This work was supported by an Incheon National University Research Grant in 2023 (20230059).

Data Availability Statement: No data were used to support this study.

Conflicts of Interest: The authors declare no conflict of interest.

References

1. Yoon, J.Y.; Singh, R. Effect of the multi-staged clutch damper characteristics on the transmission gear rattle under two engine conditions. *Proc. Inst. Mech. Eng. Part D J. Automob. Eng.* **2013**, *227*, 1273–1294. [[CrossRef](#)]
2. Guo, D.; Zhou, Y.; Zhou, Y.; Wang, Y.; Chen, F.; Shi, X. Numerical and experimental study of gear rattle based on a refined dynamic model. *Appl. Acoust.* **2022**, *185*, 108407. [[CrossRef](#)]

3. Zhou, Y.; Shi, X.; Guo, D.; Dazer, M.; Bertsche, B.; Mei, Z. Experimental investigation of gear rattle and nonlinear dynamic interaction in a dual-clutch transmission. *Appl. Acoust.* **2023**, *204*, 109233. [[CrossRef](#)]
4. Diez-Ibarbia, A.; Fernandez-del-Rincon, P.; Garcia, P.; Viadero, F. Gear rattle dynamics under non-stationary conditions: The lubricant role. *Mech. Mach. Theory* **2020**, *151*, 103929. [[CrossRef](#)]
5. Bozca, M. Transmission error model-based optimization of the geometric design parameters of an automotive transmission gearbox to reduce gear-rattle noise. *Appl. Acoust.* **2018**, *130*, 247–259. [[CrossRef](#)]
6. Rigaud, E.; Liaudet, J.P. Investigation of gear rattle noise including visualization of vibro-impact regimes. *J. Sound Vib.* **2020**, *467*, 115026. [[CrossRef](#)]
7. Donmez, A.; Kahraman, A. Influence of various manufacturing errors on gear rattle. *Mech. Mach. Theory* **2022**, *173*, 104868. [[CrossRef](#)]
8. Singh, R.; Xie, H.; Comparin, R.J. Analysis of automotive neutral gear rattle. *J. Sound Vib.* **1989**, *131*, 177–196. [[CrossRef](#)]
9. Pizzolante, F.; Battarra, M.; D’Elia, G.; Mucchi, E. A rattle index formulation for single and multiple branch geartrains. *Mech. Mach. Theory* **2021**, *158*, 104246. [[CrossRef](#)]
10. Guo, D.; Ning, Q.; Ge, S.; Wang, Y.; Zhou, Y.; Shi, X. Nonlinear characteristic analysis of gear rattle based on refined dynamic model. *Nonlinear Dyn.* **2022**, *110*, 3109–3133. [[CrossRef](#)]
11. Shangguan, W.B.; Liu, X.L.; Yin, Y.; Rakheja, S. Modeling of automotive driveline system for reducing gear rattles. *J. Sound Vib.* **2018**, *416*, 136–153. [[CrossRef](#)]
12. Trochon, E.P. Analytical Formulation of Automotive Drivetrain Rattle Problems. Master’s Thesis, The Ohio State University, Columbus, OH, USA, 1997.
13. Idehara, S.J.; Flach, F.L.; Lemes, D. Modeling of nonlinear torsional vibration of the automotive powertrain. *J. Vib. Control.* **2018**, *24*, 1774–1786. [[CrossRef](#)]
14. Beinstingel, A.; Parker, R.G.; Marburg, S. Experimental measurement and numerical computation of parametric instabilities in a planetary gearbox. *J. Sound Vib.* **2022**, *536*, 117160. [[CrossRef](#)]
15. Pizzolante, F.; Battarra, M.; Mucchi, E. The role of gear layout and meshing phase for whine noise reduction in ordinary geartrains. *Mech. Mach. Theory* **2023**, *181*, 105209. [[CrossRef](#)]
16. Palermo, A.; Britte, L.; Janssens, K.; Mundo, D.; Desmet, W. The measurement of Gear Transmission Error as an NVH indicator: Theoretical discussion and industrial application via low-cost digital encoders to an all-electric vehicle gearbox. *Mech. Syst. Signal Process.* **2018**, *110*, 368–389. [[CrossRef](#)]
17. Mughal, H.; Sivayogan, G.; Nader, D.; Ramin, R. An efficient analytical approach to assess root cause of nonlinear electric vehicle gear whine. *Nonlinear Dyn.* **2022**, *110*, 3167–3186. [[CrossRef](#)]
18. Yoo, H.G.; Chung, W.J.; Kim, B.S.; Park, Y.J.; Kang, M.R.; Lee, H.K.; Kim, M.S.; Lee, K.S. Effect of hybrid metal-composite gear on the reduction of dynamic transmission error. *J. Mech. Sci.* **2023**, *37*, 3445–3457. [[CrossRef](#)]
19. Barthod, M.; Hayne, B.; Tébec, J.L.; Pin, J.C. Experimental study of gear rattle excited by a multi-harmonic excitation. *Appl. Acoust.* **2007**, *68*, 1003–1025. [[CrossRef](#)]
20. Cui, L.; Liu, T.; Huang, J.; Wang, H. Improvement on meshing stiffness algorithms of gear with peeling. *Symmetry* **2019**, *11*, 609. [[CrossRef](#)]
21. Chen, L.; Zhang, X.; Yan, Z.; Zeng, R. Matching model of dual mass flywheel and power transmission based on the structural sensitivity analysis method. *Symmetry* **2019**, *11*, 187. [[CrossRef](#)]
22. Ren, Z.; Xin, X.; Sun, G.; Wei, X. The effect of gear meshing on the high-speed vehicle dynamics. *Veh. Syst. Dyn.* **2021**, *59*, 743–764. [[CrossRef](#)]
23. Garvey, S.D.; Penny, J.E.T.; Friswell, M.I. The relationship between the real and imaginary parts of complex modes. *J. Sound Vib.* **1998**, *212*, 75–83. [[CrossRef](#)]
24. Rubens, G.S.J. Advanced in the Theory of Linear Dynamical Systems through Coordinate Decoupling. Ph.D. Thesis, University of California, Berkeley, CA, USA, 2019.
25. Tisseur, F.; Meerbergen, K. The quadratic eigenvalue problem. *SIAM Rev.* **2006**, *43*, 235–286. [[CrossRef](#)]
26. Afolabi, D. Linearization of the quadratic eigenvalue problem. *Comput. Struct.* **1987**, *26*, 1039–1040. [[CrossRef](#)]
27. Chen, H.C.; Taylor, R.L. Solution of eigenproblems for damped structural systems by the Lanczos algorithm. *Comput. Struct.* **1988**, *30*, 151–161. [[CrossRef](#)]
28. Datta, B.N.; Elhay, S.; Ram, Y.M. Orthogonality and partial pole assignment for the symmetric definite quadratic pencil. *Linear Algebra Appl.* **1997**, *257*, 29–48. [[CrossRef](#)]
29. Golub, G.H. Some modified matrix eigenvalue problems. *SIAM Rev.* **1973**, *15*, 318–334. [[CrossRef](#)]
30. Arnoldi, W.E. The principle of minimized iterations in the solution of the matrix eigenvalue problem. *Q. Appl. Math.* **1951**, *9*, 17–29. [[CrossRef](#)]
31. Den Hartog, J.P. *Mechanical Vibrations*; Dover Publications: New York, NY, USA, 1985.
32. Inman, D.J. *Engineering Vibration*; Pearson Education Asia: Seoul, Korea, 2013.
33. Luis, J.; Zabala, M.; All, M.; Connor, J.J.; Sussman, J.M. State-Space Formulation for Structural Dynamics. Master’s Thesis, Massachusetts Institute of Technology, Cambridge, MA, USA, 1996.

34. Koch, U.; Wiedemann, D.; Sundqvist, N.; Ulbrich, H. State-space modelling and decoupling control of electromagnetic actuators for car vibration excitation. In Proceedings of the IEEE 2009 International Conference on Mechatronics, ICM 2009, Málaga, Spain, 14–17 April 2009.
35. Leonard, I.E. The matrix exponential. *SIAM Rev.* **1996**, *38*, 507–512. [[CrossRef](#)]
36. Bay, J. *Fundamentals of Linear State Space Systems*; WCB McGraw-Hill: Boston, MA, USA, 1999.
37. Macías, J.A.R.; Expósito, A.G.; Soler, A.B. A comparison of techniques for state-space transient analysis of transmission lines. *IEEE Trans. Power Deliv.* **2005**, *20*, 894–903. [[CrossRef](#)]
38. Rook, T.E.; Singh, R. Modeling of automotive gear rattle phenomenon: State of the art. *J. Passeng. Cars* **1995**, *104*, 2332–2343.
39. Padmanabhan, C.; Barlow, R.C.; Rook, R.C.; Singh, R. Computational issues associated with gear rattle analysis. *J. Mech. Des.* **1995**, *117*, 185–192. [[CrossRef](#)]
40. Curtis, S.; Pears, J.; Palmer, D.; Eccles, M.; Poon, A.; Kim, M.G.; Jeon, G.Y.; Kim, J.K.; Joo, S.H. An analytical method to reduce gear whine noise, including validation with test data. *J. Passeng. Car Mech. Syst.* **J.** **2005**, *114*, 2195–2202.

Disclaimer/Publisher’s Note: The statements, opinions and data contained in all publications are solely those of the individual author(s) and contributor(s) and not of MDPI and/or the editor(s). MDPI and/or the editor(s) disclaim responsibility for any injury to people or property resulting from any ideas, methods, instructions or products referred to in the content.